Research Square

Preprints are preliminary reports that have not undergone peer review.
They should not be considered conclusive, used to inform clinical practice,
or referenced by the media as validated information.

Biomimetic Design of Manganese-Doped Carbon Dot Nanozymes with Ultrahigh SOD-Like Activity for ALS Management

Kelong Fan

fankelong@ibp.ac.cn

Institute of Biophysics, Chinese Academy of Sciences https://orcid.org/0000-0001-6285-1933

Yaxin Hou

Institute of Biophysics, Chinese Academy of Sciences

Xuejiao Gao

College of Chemistry and Chemical Engineering, Jiangxi Normal University https://orcid.org/0000-0001-7007-4417

Jing Li

Chongqing University

Guoheng Tang

Institute of Biophysics, Chinese Academy of Sciences https://orcid.org/0009-0000-8010-1220

Qizhi Wang

Institute of Zoology, Chinese Academy of Sciences

Wenwen Yang

Shenzhen Polytechnic University

Qing Xie

Chongqing University

Ran Xu

Institute of Biophysics, Chinese Academy of Sciences

Dong Liu

Shenzhen Polytechnic University

Liming Wang

Institute of High Energy Physics, Chinese Academy of Sciences https://orcid.org/0000-0003-1382-9195

Yujing Ren

Northwestern Polytechnical University https://orcid.org/0000-0002-0851-8248

Qingying Luo

Shenzhen Polytechnic University

Cui Liu

Chongqing University https://orcid.org/0000-0002-8399-5765

Lei Li

Institute of Zoology, Chinese Academy of Sciences https://orcid.org/0000-0001-5478-5681

Article

Keywords:

Posted Date: May 5th, 2026

DOI: https://doi.org/10.21203/rs.3.rs-6356438/v1

License: This work is licensed under a Creative Commons Attribution 4.0 International License.
Read Full License

Additional Declarations: There is **NO** Competing Interest.

Abstract

Amyotrophic lateral sclerosis (ALS) is a devastating neurodegenerative disease without cure. Reactive oxygen species (ROS)-induced oxidative stress and mitochondrial dysfunction are considered critical factors in ALS pathogenesis. Here, we design carbon dot superoxide dismutase (SOD) nanozymes with manganese doping (Mn@CDs) by screening for the optimal active site according to the special structures of natural SODs. Mn coordinates with N and O in the CD scaffold, optimizing its structure, enhancing electron transfer and superoxide anion binding, and achieving superhigh specific activity of more than 7×10^4 U/mg. Theoretical calculations reveal the SOD-like activity of Mn@CDs from both kinetic and thermodynamic perspectives, identifying MnN_2O_2 (with amide-derived N) as the most likely active center. Unlike previous single-atom nanozymes with planar structures, this active center exhibits a coordination environment and a non-planar spatial conformation that closely resembles the active site of natural MnSOD enzymes. After being applied in ALS therapy, Mn@CDs effectively prevent oxidative stress and protect mitochondria from abnormalities in morphology, quantity, and function. Hence, administration of Mn@CDs prolonged survival by 14.5 days, with a 93% increase over the effect of edaravone. These results suggest that Mn@CDs hold significant potential as a promising therapeutic candidate for ALS treatment.

Introduction

Amyotrophic lateral sclerosis (ALS), which is characterized by progressive motor deficits and fatal respiratory failure, is a severe neurodegenerative disease without a cure and claims at least 30,000 lives worldwide each year[1–3]. Although the underlying pathogenesis of ALS has not been fully elucidated, emerging evidence has emphasized the critical role of oxidative stress in ALS disease progression[4,5]. A prototypical example is the ALS caused by superoxide dismutase 1 (SOD1) mutations. This type of ALS is known as the loss or impairment of the original antioxidant function of SOD1, leading to the accumulation of oxidative damage in motor neurons and muscles[6]. Edaravone (Eda), a small molecule with excellent reactive oxygen species (ROS)-scavenging activity, has once been positioned as one of the most promising drugs for ALS therapy. Unfortunately, after Eda was approved by the Food and Drug Administration (FDA), a considerable proportion of ALS patients did not experience resolution of symptoms in clinical datasets, and many studies have reported that Eda did not prolong survival in these patients[7,8]. In this context, there is a pressing need to develop novel antioxidant therapies against ALS with superior efficacy. In addition to oxidative stress, mitochondrial dysfunction is another pivotal mechanism in ALS pathogenesis. Since the high energy demand of motor neurons must be met by a large complement of mitochondria, mitochondrial abnormalities can lead to severe impairments in the motor function of ALS patients[9]. Importantly, the increased ROS level inflicts damage upon mitochondria. Subsequently, dysfunctional mitochondria further contribute to the formation of ROS, thereby initiating a vicious cycle that exacerbates oxidative stress in motor neurons and muscles[10].

Nanotechnology has dramatically changed the pharmaceutical and biotechnology industries[11]. Nanotechnology significantly improves the pharmacokinetics of drug molecules by protecting them from the rapid decay of their antioxidant activity due to harsh environmental influences[12,13]. Recently, the application of nanomaterials in ALS therapy is under expansion and continuous development[14–16]. Importantly, since the discovery of superoxide dismutase activity in fullerenes[17], many nanomaterials with enzyme-like activity have been developed for scavenging reactive oxygen species[18–20]. These nanomaterials with intrinsic enzyme-like catalytic activities have been named nanozymes by our group[21,22]. Nanozymes have been widely used in biomedical fields because of their advantages of low cost, high stability, and ease of manipulation[19,23]. Nevertheless, the low catalytic activity of nanozymes is still a key limitation for their practical application. To improve their catalytic efficiency, the new concept of "single-atom catalysis" has been introduced into nanozymes, producing single-atom nanozymes. Many single-atom nanozymes, such as Cu single-atom nanozymes[24], noble metal-porphyrin MOF single-atom nanozymes (M**x**P, **x** stands for Pt, Pd, Ru, and Ir)[25], Mn single-atom nanozymes[26], Ag-TiO_2 single-atom nanozymes[27], and Co single-atom nanozymes[28], have been developed and applied in tumor treatment, wound antimicrobial, and anti-inflammatory applications. Although single-atom nanozymes have been developed rapidly in the last five years from preparation to modulation to application, their catalytic performance is still far from satisfactory as a substitute for that of natural enzymes. In addition, most single-atom nanozymes inevitably contain catalytic sites with multiple structures during the preparation process due to substrate heterogeneity and coordination inhomogeneity, resulting in a decrease in catalyst activity and specificity[29–31]. In addition, biocompatibility is a key issue limiting the application of single-atom nanozymes in biomedicine. Therefore, the use of biocompatible support materials to ensure atom dispersion, stable anchoring, and high loading of metal active sites are urgent challenges to be solved in the application of these materials in the field of nanobiomedicine.

Carbon dots (CDs) are a class of fluorescent carbon nanomaterials with a particle size of less than 10 nm[32]. They have shown broad applications in bioimaging, sensing, and catalysis because of their biocompatibility, easy synthesis, low cost, and unique fluorescent properties[33–36]. In recent years, the biocatalytic activity of CDs has also attracted attention. The peroxidase-like activity of CDs has been widely used in biochemical sensing, antibacterial, and antitumor applications[37–39]. Moreover, CDs with antioxidant activity have also shown great potential in cell protection, anti-inflammatory, and antiaging applications[40–44]. Surface groups such as the carboxyl, hydroxyl, carbonyl, and amino groups of CDs are beneficial for binding with substrates through hydrogen bonding, electrostatic forces, *etc.*, promoting electron transfer and enabling high catalytic activity. In our previous work, we prepared CD nanozymes with activities exceeding those of natural SOD[44]. CD nanozymes with good fluorescence properties, SOD-like activity and inflammation targeting ability were subsequently designed through a surface structure modulation strategy, realizing the dual functions of *in vivo* inflammation treatment and bioimaging[43].

Most natural enzymes are proteins composed of amino acids linked by amide bonds. The presence of metal ions is required for almost one-third of known natural enzymes to exhibit catalytical activity. Among them, metalloenzymes have tightly bound metal ions, and these tightly bound metal ions in enzymes are usually the catalytically active centers. Metal ions carry out multiple processes, such as electron transfer, substrate binding/recognition, and catalysis at the active site of metalloenzymes. It is worth noting that the functional groups of CDs can coordinate with, or even form chelates with, a variety of metal ions, which is similar with the coordination interaction between metal ions and proteins in metalloenzymes. The biomimetic metal-CD nanozymes with high catalytic performance may be designed by combining CDs with metal ions. To date, four types of SOD have been identified: Cu, Zn SOD, Mn SOD, Fe SOD, and Ni SOD. Therefore, we investigated the effects of doping CDs with these types of metal ions and other metal ions (derived from reported metal nanoparticles or metal oxide nanoparticles with SOD-like activity) on the SOD-like activity of CD nanozymes. By comparing their SOD-like activities, the Mn-doped CDs (Mn@CDs) were screened out, which exhibited the optimal SOD-like activity of over 7×10^4 U/mg (Fig. 1). The structural characterization results revealed that the introduction of single Mn atoms altered the local coordination geometry and surface structure of the CDs via coordination with N/O-containing groups. This, in turn, affected the electronic structure of the Mn@CDs as a whole, thereby contributing to their high catalytic activity. The coordination of Mn^{2+} with precursors alter the formation process of the CDs, leading to the conversion of the enol to the ketone structure in the CDs, a reduction in N content, and an increase in amide bond content. The coordination of Mn with the O/N-containing groups of the CDs promotes electron transfer between Mn and CD skeleton, leading to the coexistence of Mn^{2+} and Mn^{3+} in Mn@CDs. This enables the Mn^{2+}/Mn^{3+} valence cycle during the catalysis of $O_2^{\bullet-}$ dismutation. Moreover, the coordination between Mn and carboxyl/amino/hydroxyl groups of CD skeleton decreases the degree of hydrogen bonding with hydrogen peroxide and accelerates the desorption of the catalytic products. The coordination number of Mn is unsaturated, and Mn readily binds to superoxide anions. These effects ultimately synergistically enhanced the SOD-like activity. Theoretical calculations further validated our speculations. This nanozyme with excellent SOD-like activity was subsequently applied for ALS treatment research. Both *in vitro* and *in vivo* experiments revealed that Mn@CDs robustly scavenged ROS and mitigated oxidative stress, effectively protected mitochondria from abnormalities in morphology, quantity, and function. As a result, the administration of the Mn@CDs successfully protected motor neurons from degeneration, ameliorated the defects in neuromuscular junctions, rescued the atrophy of muscle units, and inhibited gliosis, thereby improving the motor behavior of the ALS model mice. More importantly, compared with the vehicle control, Mn@CD treatment significantly prolonged the survival time from 160 days to 174.5 days, with a 93% increase over the effect of Eda treatment. In summary, we have demonstrated the potential of nanozyme-based antioxidant therapy for the treatment of ALS.

Results and Discussion

Preparation and characterization of the Mn@CDs

In our previous work, we prepared CDs with good SOD activity via a solvothermal method in which folic acid, formamide and glutathione were used as raw materials[43]. The CDs contain abundant nitrogen- and oxygen-containing functional groups that can be involved in catalyzing the superoxide anion disproportionation. Moreover, these functional groups can be efficiently coordinated with metal ions. The UV-vis absorption spectra of CDs before and after adding metal ions were measured here. As shown in Supplementary Fig. 1, in the presence of these metal ions, the position of the absorption peak of the CDs has shifted significantly, and the intensity of the absorption peak has also changed remarkably, indicating that CDs could coordinate with these metal ions. It is reasonable to believe that metal ions are able to change the surface structure and local coordination geometry of CDs through coordination, which is similar to the interaction between metal ions and proteins in metalloenzymes. Therefore, we investigated whether we could obtain higher SOD-like activity by constructing metal sites in the skeleton of CDs to mimic metalloenzymes. According to the four known types of SOD (Cu, Zn SOD, Mn SOD, Fe SOD, and Ni SOD) and the reported metal-containing nanoparticles with SOD-like activity, we prepared 12 kinds of metal doped CDs using formamide, glutathione and metal ions (Cu, Zn, Mn, Fe, Ni, Mg, Ru, Mo, Sn, Au, Pt, or Pd) as raw materials. We determined the metal loading of these metal-doped CDs using inductively coupled plasma optical emission spectroscopy (ICP-OES). As shown in Supplementary Table 1, the metal loading amounts exhibit significant variation under the same metal feeding amount. This may be because some metals (such as Ni, Sn, Au, Pd) fail to form stable coordination bonds with CD precursors during the reaction, hindering the stable loading. It can be seen that most metals here exhibited excessively low loading amounts or limited effects on regulating the SOD-like activity of CDs (detailed discussion in Supplementary Information). Obviously, Mn@CDs exhibited much higher SOD-like activity than the others (Supplementary Fig. 2). So, the Mn@CDs were further studied.

Transmission electron microscopy (TEM) images (Fig. 2a) displayed that these Mn@CDs exhibited good monodispersity, with an average particle size of 2.0 ± 0.4 nm (Supplementary Fig. 3). As shown in Supplementary Fig. 4, Mn@CDs exhibited a negative zeta potential of − 38 mV, indicating their high colloidal stability. The loading amount of Mn in the Mn@CDs could be tuned by adjusting the dose of $Mn(ClO_4)_2{\cdot}6H_2O$ used in the synthesis process (12.5, 25, 50, and 100 mg). As the dose of $Mn(ClO_4)_2{\cdot}6H_2O$ increased from 12.5 to 100 mg, the loading amounts of Mn increased from 1.5% to 5.4% (Supplementary Table 2, determined by ICP—OES), much greater than those of many Mn single-atom nanozymes, indicating that CDs could provide higher Mn loading. In our latest work[45], we have revealed the tautomerism between enol and ketone structures in the CDs without metal doping (donated as CDs in the following text). The fluorescence spectrum of the CDs showed an optimal peak at 684 nm with a shoulder peak at 652 nm, corresponding to the fluorescence emission of the ketone and enol forms, respectively, of CDs[45]. As the amount of doped Mn increased, the fluorescence intensity of the Mn@CDs decreased significantly, and the magnitude of the decrease in the peak at 684 nm was much greater than that at 652 nm (Fig. 2b). These results suggested that the Mn coordinated with ketone structure in CDs and then facilitated the transformation from enol to ketone, thus changing the energy levels of their electronic excited states, which ultimately led to change in the emission spectrum.

To investigate the interaction between CDs and doped Mn, particularly the effect of Mn doping on the structure of CDs, UV-vis absorption spectroscopy, Fourier transform infrared (FT-IR) spectroscopy, proton nuclear magnetic resonance (^{1}H-NMR) spectroscopy, and X-ray photoelectron spectroscopy (XPS) were employed. As shown in the UV-vis absorption spectra (Fig. 2c), CDs exhibited obvious absorption peaks at 420, 603, 627, and 678 nm. The absorption peak at 420 nm increased significantly in 1 mM NaOH solution and decreased significantly in 1 mM HCl solution (Fig. 2d), indicating that it can be attributed to enol form structure of CDs. In contrast, the absorption peak at 678 nm was blue-shifted to 638 nm in NaOH solution (Fig. 2d), suggesting that the peaks at 678 and 638 nm were related to the ketone and enol structures, respectively, of CDs. When the polarity of the solvent decreases, the position of π→π* transition absorption peak displays a blue shift, while that of n→π* transition absorption peak displays a red shift. As shown in Fig. 2e, compared with the UV-vis absorption spectrum of CDs in water, the absorption peaks at 408 and 420 nm of CDs displayed a blue shift, while those at 603, 627 and 678 nm all underwent a red shift in THF (99.6%). This phenomenon indicated that the absorption peak at 420 nm was attributed to the π→π* transitions of enol form in CDs. The peaks at 678 nm were attributed to the n→π* transitions of ketone in CDs, and the peak at 638 nm was attributed to the n→π* transition of the enol structure. With the increase in Mn doping amount, the absorption peak at 420 nm was clearly red-shifted to 447 nm, accompanied by a decrease in the absorbance (Fig. 2c), while a new peak at 350 nm appeared. In addition, the absorption peaks at 627 and 678 nm were red-shifted to 650 and 700 nm, respectively. Furthermore, under alkaline conditions (1 mM NaOH solution), the peak at 447 nm of Mn@CDs increased significantly, the peak at 350 nm was red-shifted to 390 nm, while that at 700 nm was blue-shifted to 656 nm (Fig. 2f), indicating that the absorption peaks at 447 and 656 nm were ascribed to the π→π* and n→π* transition, respectively, of the enol structure in Mn@CDs, while the peaks at 350 and 700 nm was the π→π* and n→π* transition absorption, respectively, of ketone structure. It's of note that the enhancement degree (1.39-fold) of the peak at 447 nm of Mn@CDs in 1 mM NaOH was much lower than that peak at 420 nm of CDs (1.93-fold) (Figs. 2d and f). The ratio of $A_{420\ nm}/A_{678\ nm}$ of CDs (2.8) in water was much higher than the ratio of $A_{447\ nm}/A_{700\ nm}$ of Mn@CDs (1.7). These results indicated that coordination of Mn caused a decrease in the enol content and an increase ketone content in CDs. Therefore, we speculated that Mn doping promoted the conversion of the enol to the ketone structure in CDs may due to ketone has higher coordination affinity for Mn.

FT-IR spectra of CDs and Mn@CDs are shown in Supplementary Fig. 5. The absorption bands at 3180 and 3400 cm^{-1} were assigned to the stretching vibrations of N-H and O-H, respectively. After Mn doping, the intensity of the characteristic absorption peak for N-H decreased. Moreover, elemental analysis result (Supplementary Table 3) revealed that Mn doping significantly induced the decrease of N content in CDs, indicating that the introduction of Mn may affect the doping of N atoms during the formation of CDs. The peaks at 1680 and 1600 cm^{-1} correspond to the stretching vibrations of C = O (ketone, carboxyl, or amide groups) and C = C/C = N, respectively. Upon Mn incorporation into CDs, the peak at 1600 cm^{-1} gradually shifted toward higher wavenumbers, indicating that Mn may coordinate with N-containing heterocycles in the CDs. Additionally, the absorption of characteristic peaks at 1550 cm^{-1} (amide II band, N-H bending vibrations) and 1308 cm^{-1} (amide III band, C-N stretching vibrations)

gradually increased along with the increase of Mn content. This result suggests that Mn doping may lead to an increase in amide bond content, or Mn ions may coordinate with amide groups and therefore reduce the symmetry and increase the force constant. The proton magnetic resonance (^{1}H-NMR) spectra were also used to reveal the structure of Mn@CDs (Supplementary Fig. 6). The characteristic peaks for aliphatic hydrocarbons appeared in the range of 1.0–1.8 ppm, while peaks in the range of 2.0–2.5 ppm were assigned to α-H to carbonyls in ketones/acids or with allylic/benzylic protons. Peaks in the range of 2.6–3.2 ppm were assigned to N–CHx, and peaks in the range of 3.3–4.2 ppm can be attributed to protons α to C–O (i.e., α-H of O-containing functional groups such as alkoxy or hydroxyl). Peaks at 8 ppm indicated the presence of aromatic hydrogen. Moreover, the peaks at approximately 5.5 ppm may be attributed to alkenyl hydrogen, heteroaromatic or heteroatom-adjacent proton of CDs. In our previous work[45], the resonance at ~ 5.5 ppm of CDs without metal doping significantly increased under alkaline condition (0.01 M NaOD). Therefore, the alkenyl protons make a great contribution to this resonance peak. The peak at ~ 4.8 ppm was assigned to the residual HDO peak from the D_2O solvent. This peak gradually broadened after Mn introduction, a phenomenon that may have stemmed from the influence of the paramagnetic properties of $Mn^{2+/3+}$ on the ^{1}H-NMR spectrum. As a paramagnetic ion, $Mn^{2+/3+}$ possesses unpaired electrons that accelerate the relaxation rate of surrounding protons, thereby resulting in peak broadening. The attenuation or disappearance of peaks of aliphatic, alkenyl, or aromatic protons may be the consequences of paramagnetic relaxation of $Mn^{2+/3+}$. Nonetheless, the possibility that these structural alterations arise from Mn doping cannot be excluded, which could be proved by other structural characterization methods including UV-vis absorption, FT-IR, and XPS spectroscopy.

XPS was used to further analyze the coordination of the CD scaffold with Mn. As shown in Supplementary Fig. 7, the XPS survey of Mn@CDs exhibited five peaks at 645, 532, 400, 285, and 163 eV ascribing to Mn 2p, O 1s, N 1s, C 1s, and S 2p, respectively. The Mn 2p XPS spectra of all the Mn@CD samples loaded with different amounts of Mn exhibited two peaks at binding energies of ~ 640 and ~ 654 eV, corresponding to Mn $2p_{3/2}$ and Mn $2p_{1/2}$, respectively (Supplementary Fig. 8). The Mn 2 $p_{3/2}$ peak can be well fitted with two peaks at 640.4 and 642.3 eV, attributed to Mn^{2+} and Mn^{3+}, respectively. In our recent research work[45], we conducted an in-depth investigation into the interaction between Mn^{2+} and CDs. The XPS of the mixture of Mn^{2+} and CDs also displayed a significant signal of Mn^{3+}. The C 1s, O 1s, and N spectra of CDs showed obvious shifts in peak positions in the presence of Mn ions. Therefore, we speculated that the coordination between Mn^{2+} and the surface structure of CDs leads to the partial transfer of electrons from the Mn^{2+} to the surface groups of CDs. This electron transfer increases the binding energy of Mn, which in turn results in the appearance of the signal of Mn^{3+}. Similar phenomenon appeared in Mn@CDs. As shown in Fig. 2g, the C1s spectra of Mn@CDs revealed that after Mn doping, the carbon content with the highest binding energy (i.e., C = N, C = O, O–C = O, and N–C = O) decreased, while the carbon content with medium binding energy (i.e., C–O and C–N) increased. Additionally, the binding energies of both types of carbon decreased. This indicated that after coordination with Mn, the electron density around carbon atoms increased due to Mn transferring part of its electrons to carbon-containing groups. This behavior can be understood in terms of ligand–metal charge redistribution:

coordination of Mn(II) with the C = N/C = O groups in the CDs leads to partial transfer of electron density from Mn to these carbon-based ligands, which is consistent with the increase in the binding energy of Mn and the decrease in the binding energy of C. Moreover, the red-shift of π→π* transition absorption of Mn@CDs (Fig. 2c) also conformed this. The high resolution (HR) N 1s spectra (Fig. 2h) showed that Mn doping led to the increase of content of N with low binding energy (i.e., pyridinium), indicating that the nitrogen-containing groups of CDs coordinate with Mn atoms and accept their electrons. Moreover, the binding energy of pyrrolic N gradually decreased, suggesting that pyrrolic N also coordinated with Mn and formed backbonding π-bond. In contrast, the HR O 1s XPS spectra (Fig. 2i) revealed that the content of O with higher binding energy increased significantly, confirming Mn coordination with oxygen-containing groups of CDs and accept their electrons. The S 2p XPS spectra of these Mn@CDs were deconvoluted into peaks corresponding to thiol groups, $2p_{3/2}$ and $2p_{1/2}$ of thiophene sulfur, and oxidized sulfur ($–C–SO_{x–}$, x = 2–4) at 162.1, 163.8, 164.9, and 168.5 eV, respectively (Supplementary Fig. 9)[46,47]. Furthermore, with the increase in Mn doping, the content of thiols gradually decreased, while that of oxidized sulfur increased, indicating that Mn ions induce the oxidation of thiol groups in GSH during the reaction, thereby altering the structure of CDs. Therefore, we speculate that Mn(II) coordinates with the O/N-containing groups (i.e., C = N, C = O, O—C = O, N—C = O, pyrrole and pyridinium) of CDs. The empty orbitals of Mn that coordinate with O atoms (in—OH or C—O) and pyridinic N accept the lone pairs of electrons from O or N to form coordinate bonds. In contrast, another part of the Mn coordinates with C = O, C = N, or pyrrole, transferring electrons to the empty π orbitals of the ligand groups to form backdonation π bonds. This process not only resulted in the coexistence of Mn^{2+} and Mn^{3+} but also caused significant changes in the structure, such as surface structure and local coordination geometry, of CDs.

The electron spin resonance (ESR) was employed to verify whether the Mn^{2+}/Mn^{3+} valence cycling exists in Mn@CDs during the catalytic reaction of $O_2^{\bullet-}$ dismutation. The xanthine-xanthine oxidase system was employed to generate $O_2^{\bullet-}$. Xanthine oxidase and Mn@CDs were added to the xanthine solution, and the Mn^{2+} signals in the system were detected immediately. The results showed that compared with the control group consisting of Mn@CDs and xanthine, the Mn^{2+} signal of the aforementioned reaction system decreased significantly (Supplementary Fig. 10), which indicated that the valence state of Mn in Mn@CDs increased during the catalytic reaction of $O_2^{\bullet-}$ dismutation. After the mixed system was incubated for 10 min, Mn^{2+} signal recovered to that of the control group, showing that when the reaction approached completion, the valence state of Mn could approximately revert to its initial state. These phenomena directly confirmed that the valence cycling process between Mn^{2+} and Mn^{3+} occurs in Mn@CDs during the catalysis of $O_2^{\bullet-}$ dismutation, which is analogous to the catalytic mechanism of cerium oxide nanozymes. Therefore, the coexistence of Mn with two valences and the changed structure of CDs induced by Mn doping enhance the catalytic capacity of the Mn@CDs.

In the XRD pattern (Supplementary Fig. 11), a diffraction peak at approximately 22–25° corresponding to the 002 facet of graphite was observed, whereas the signals of metallic Mn or Mn-oxide nanoparticles

were not, suggesting the potential formation of single Mn atoms in the CD scaffold. High-angle annular dark-field scanning transmission electron microscopy (HAADF-STEM) was employed to confirm the atomic dispersion of the Mn atoms. As shown in Fig. 3a, high-density bright dots highlighted with red circles were observed in the CDs, revealing the formation of Mn single-atom sites. Energy-dispersive X-ray spectroscopy (EDS) mapping (Fig. 3b) confirmed the uniform distribution of C and Mn atoms over the Mn@CDs.

X-ray absorption fine structure (XAFS) was utilized to investigate the local electronic structure and coordination information at the atomic level of the Mn@CDs. As shown in the X-ray absorption near-edge structure (XANES) spectra at the Mn K-edge (Fig. 3c), the absorption threshold of the Mn@CDs was located between those of MnO and Mn_2O_3, implying that the valence state of Mn was + 2 ~ 3, which coincides with the XPS results. The Mn K-edge Fourier transform extended X-ray absorption fine structure (FT-EXAFS) of the Mn@CDs and reference samples are shown in Fig. 3d. The FT-EXAFS spectrum of the Mn@CDs exhibited a predominant scattering peak at 1.6 Å, which can be assigned to the first-shell Mn-N/O coordination. Mn—Mn bonding at 2.3 Å was not observed, implying atomically dispersed Mn in the Mn@CDs. The wavelet transforms (WTs) of the Mn Kedge EXAFS oscillations are displayed in Fig. 3e. Compared with the spectra of the Mn foil and Mn_2O_3, the WT of the Mn@CDs exhibited a major feature centered at 3.8 $Å^{-1}$, which was attributed to Mn-N(O) bonds. However, the absence of the signal belonging to Mn-Mn (~ 6.0 $Å^{-1}$) rules out the existence of aggregated Mn species. Quantitative least-squares FT-EXAFS curve fitting analysis was performed to better reveal the coordination environment and structural parameters around the single-atom Mn center. The best-fit results clearly show that the Mn-N/O coordination number of the first layer of Mn atoms in the Mn@CDs was approximately 4.2 (Fig. 3f). Therefore, we can speculate that Mn exists in CDs as a single atom through coordination with 4 ~ 5 N/O atoms. The presence of a large proportion of Mn(III) suggests the electron transfer process between Mn and CDs, which is potentially very useful for electron transfer in catalytic processes.

The optimal SOD-like activity of Mn@CD reached more than $7×10^4$ U/mg (Fig. 3g), much higher than other metal doped CDs (e.g. Zn@CDs and Mg@CDs, Supplementary Fig. 12). To the best of our knowledge, this is the highest specific activity of SOD nanozymes reported thus far. The ESR results (Fig. 3h-i) revealed that the Mn@CDs were capable of scavenging the source of ROS (superoxide anion) and the most toxic ROS (hydroxyl radicals), indicating that the Mn@CDs have high potential for the treatment of oxidative stress-related diseases. Moreover, the Mn@CDs exhibited good stability in SOD-like activity in the temperature ranging from 20 to 45°C and pH ranging from 4 to 10 (Supplementary Figs. 13a and b), indicating that Mn@CDs can be applied to most biological system environments, including inflammatory microenvironments. Additionally, we investigated the SOD-like activity, fluorescence and UV-vis absorption spectra of Mn@CDs in different media to evaluate the long-term stability of Mn@CDs. As shown in Supplementary Figs. 13c and 14, after 5 days, these properties of Mn@CDs remain basically unchanged in pure water, PBS buffer, and fetal bovine serum (FBS), indicating the good long-term stability of Mn@CDs.

Unraveling the mechanisms underlying the superhigh SOD-like activity of Mn@CDs

We performed theoretical calculations to explore the structure and mechanism of the active centers responsible for the SOD-like activity of the Mn@CDs. First, the periodic structural models were constructed based on two key experimental observations: (1) Mn might coordinate with both pyrrole and pyridinium N in the Mn@CD material, and (2) Mn coordinates with N and O atoms, with N potentially originating from amide groups (Fig. 2d). To systematically investigate the active sites in Mn@CDs, we constructed 11 periodic structural models (Fig. 4a) rather than discrete molecular clusters. The unit cell parameters for all the models are included in Supplementary Table 4. This periodic approach was chosen primarily due to computational feasibility and the ability to clearly delineate structure–activity relationships. Given that experimentally synthesized Mn@CDs exhibit monolayer structures with an average size of approximately 2.0 ± 0.4 nm (Supplementary Fig. 3), employing cluster models would necessitate prohibitively large atomic systems (~ 200–300 atoms), significantly complicating calculations and introducing substantial structural variability, *e.g.*, edge effects, as reviewed in previous reference[48]. Periodic models effectively mitigate these issues by providing a continuous and well-defined local chemical environment, making them particularly suitable for analyzing key electronic structures and catalytic behaviors.

Furthermore, guided by experimental observations that Mn coordination involves both pyridinic and pyrrolic nitrogen atoms (as evidenced by HR N 1s spectra, Fig. 2h), our structural models separately explored these coordination environments to clearly assess their distinct effects on catalytic activity. Specifically, models **a1** – **a4** feature Mn coordinated by pyridinic nitrogen with systematically increasing oxygen coordination; models **b1** – **b4** focus on pyrrolic nitrogen coordination with a similar incremental approach to oxygen content. Additionally, models **c1** – **c3** incorporated amide coordination environments, reflecting experimentally suggested coordination scenarios (Fig. 4a). This careful design using periodic models allows us to precisely evaluate the catalytic significance of specific nitrogen coordination modes, oxygen content, and amide configurations within the Mn@CD framework.

Next, we investigated the SOD-like catalytic mechanism of Mn@CDs. In 2021, Gao and collaborators introduced the intermediate frontier molecular orbital (iFMO) model to predict nanozyme SOD activity (Fig. 4b)[49]. The iFMO refers to the molecular orbital of the nanozyme located between the reduction potentials of the two half-reactions involved in the dismutation of superoxide (φ_1 for $O_2^{\bullet-} \rightarrow O_2$ and φ_2 for $O_2^{\bullet-} + 2H^+ \rightarrow H_2O_2$), ensuring that both reactions are thermodynamically favorable. The catalytic mechanism depends critically on whether the iFMO of the nanozyme is highest occupied molecular orbital (HOMO)-mediated or lowest unoccupied molecular orbital (LUMO) -mediated. If the reaction is HOMO-mediated, the nanozyme first transfers an electron to the substrate ($O_2^{\bullet-}$), forming H_2O_2 and an electron hole (h^+), followed by electron transfer from another $O_2^{\bullet-}$ molecule to generate O_2. If the

reaction is LUMO-mediated, the nanozyme first accepts an electron from $O_2^{\bullet-}$ to generate O_2 and a charge center (e^-) and then transfers this electron to another $O_2^{\bullet-}$ molecule, producing H_2O_2 (Fig. 4b).

To determine whether the Mn@CDs in our study followed a HOMO- or LUMO-mediated mechanism, we calculated the density of states (DOS) for all 11 models and converted the energy levels into reduction electrode potentials (*E*) relative to the standard hydrogen electrode (*E* vs HE) at pH = 7. The results are shown in Fig. 4c. We find that model **a1** is semiconductor-like, **b1** is semimetallic, and the others are metallic. We marked the valence band maximum (VBM) and conduction band minimum (CBM) for the semiconductor models (representing the **HOMO** and **LUMO**, respectively) and the Fermi level for the metallic models. Only models **a1**, **b1**, and **c1** exhibited iFMOs located between φ_1 and φ_2, suggesting that they may have SOD-like activity. For **a1** and **b1**, the IFMOs are LUMOs. Among these, **c1** exhibited the highest potential for SOD activity due to its iFMO value of 0.31 V, which is closer to the optimal value of $E_{FMO} = (\varphi_1 + \varphi_2)/2$ (0.39 V).

Gao *et al.* also proposed a second standard for evaluating SOD activity on the basis of the adsorption energies of reactive oxygen species[49], specifically for determining whether $O_2^{\bullet-}$ on the nanozyme surface primarily reacts via the SOD mechanism to form H_2O_2 and O_2 rather than generating side products such as HO* (* denotes the adsorbed state) or O*. This standard is $E_{ads,HO} > -2.7$ eV and $E_{ads,H} > -3.4$ eV, where $E_{ads,HO}$ and $E_{ads,H}$ represent the adsorption energies of HO* and H* on the nanozyme surface. When these conditions are met, the SOD-like activity is favored, and the partition function $x_{SOD} > 0.5$. To evaluate this, we calculated the adsorption energies of HO* and H* for the 11 models, where HO* adsorbs on the Mn atom and H* on the N atom with the highest spin density. The results are shown in Fig. 4d. The regions where $x_{SOD} > 0.5$ are highlighted in purple, and only **c1** falls within this region, whereas **a1** and **b1** are located outside this region. Differential charge density analysis and Bader charge calculations provide insights into why **c1** exhibits the highest relative adsorption energy for OH, corresponding to the weakest adsorption affinity. The differential charge density map (Supplementary Fig. 15) reveals that charge transfer predominantly occurs between the N atom and the central Mn atom, with electrons flowing from the N atom to Mn. Although O atoms have higher electronegativity, their capacity to accept back-donated electrons is relatively weak. Consequently, as the number of O atoms increases, the valence state of the central Mn atom decreases. For instance, in the transition from A1 to A4, the Mn valence state decreases from + 1.33 to + 1.16, while in the series B1 to B4, it decreases from + 1.47 to + 1.16. As the Mn valence state decreases, the d-electron occupancy increases, leading to a shift in the energy distribution of the d orbitals toward lower energy levels. This results in a downward shift of the d-band center, thereby weakening the adsorption energy of OH. In **c1**, Mn exhibits the lowest valence state of + 1.05, which can be attributed to the presence of the amide bond that disrupts the planar structure, further weakening the coordination interaction between the N atom and the central Mn atom. Notably, this non-planar configuration more closely resembles the spatial arrangement of the active center in natural enzymes (Fig. 4e), which may be an additional factor contributing to the high SOD activity of Mn@CD materials. These results suggest that **c1** not only has the highest relative activity but

also has the best selectivity for the SOD reaction pathway, presenting the optimal active center structure. This structure features MnN_2O_2 coordination and N atoms originating from two amide groups, which is consistent with experimental observations.

In summary, the theoretical calculations provide insights into the SOD-like activity of Mn@CDs from both a kinetic perspective (iFMO model) and a thermodynamic perspective (adsorption energy model). The results suggest that the most likely active center structure for Mn@CDs is one with MnN_2O_2 coordination, where the N atoms are derived from amide groups, offering a theoretical foundation for the design of Mn-based single-atom SOD nanozymes in the future.

Antioxidant effects and mitochondrial function improvement of Mn@CDs in vitro

Mutant monomers as well as aggregates of SOD1 have been reported to reduce enzymatic activity, resulting in an accumulation of $O_2^{\bullet-}$ and triggering oxidative damage[5]. To evaluate whether Mn@CDs can reduce intracellular $O_2^{\bullet-}$ levels. NSC-34 and SH-SY5Y cells were treated with paraquat (PQ), a widely used reagent to stimulate $O_2^{\bullet-}$ production in cells. As shown in Fig. 5a and Supplementary Fig. 16, both NSC-34 and SH-SY5Y cells treated with Mn@CDs together with PQ exhibited a reduced level of dihydroethidium (DHE) fluorescence. We subsequently stimulated the cells with H_2O_2 to mimic oxidative damage and assessed the antioxidant capacity of the Mn@CDs. The fluorescence probe 2,7-dichlorofluorescein diacetate (DCFH-DA) was utilized to measure total intracellular ROS. Supplementary Figs. 17 and 18 show that the intracellular ROS level significantly increased after exposure to H_2O_2, and this increase was diminished by the addition of Mn@CDs. Additionally, confocal imaging was used to observe the ROS scavenging efficiency *in situ*. The results revealed that cells coincubated with H_2O_2 and Mn@CDs presented significantly lower ROS levels (Fig. 5b and Supplementary Fig. 19).

Dysfunction of mitochondria represents a critical stage in the pathogenesis of ALS. The burst of ROS stands as one of the primary causes of mitochondrial dysfunction. Notably, mitochondrial damage will further result in an elevation of ROS, consequently generating a ROS amplification effect[9]. In our studies, we observed that Mn@CDs are more prone to enter cells with high ROS levels (Supplementary Fig. 20). The accumulation of Mn@CDs in the cells was further quantified by confocal imaging. We found that when cells undergo oxidative damage, the uptake of Mn@CDs by the cells increases, and more importantly, these Mn@CDs could enter the mitochondria, the primary site of ROS production (Fig. 5c). This may be attributable to increased mitochondrial membrane permeability following oxidative damage[50], thereby facilitating the entry of Mn@CDs. Moreover, oxidative damage may induce a decrease in the inherent negative mitochondrial membrane potential[51], which is also beneficial to the entry of negatively charged Mn@CDs since the electrostatic repulsion is diminished (Fig. 5d). Next, we evaluated the protective effects of Mn@CDs on mitochondria. MitoSOX was used to assess the ability of the Mn@CDs to scavenge mitochondrial ROS within cells. The flow cytometry results revealed significantly lower fluorescence in the Mn@CD-treated groups than in the control groups, both in the NSC-34 and SH-SY5Y cells (Fig. 5e and Supplementary Fig. 21). Additionally, the H_2O_2 groups presented low TMRM

fluorescence, indicating decreased mitochondrial membrane potential and mitochondrial damage in NSC-34 cells. In the Mn@CD + H_2O_2 group, the Mn@CD nanozymes effectively scavenged ROS and inhibited H_2O_2-induced damage to mitochondria, resulting in negligible changes in the membrane potential (Fig. 5f). Mitochondrial damage is often accompanied by significant calcium overload, making the intracellular calcium concentration an important indicator of oxidative stress[52]. As demonstrated in this study, we further assessed intracellular calcium levels via Fluo-4 AM staining, the results of which are shown in Fig. 5g. The results showed that H_2O_2 stimulation induced pronounced calcium overload in cells, which was significantly reversed by Mn@CD treatment, reducing the percentage of calcium-overloaded cells from 42.0% to 5.06%. As ROS-induced apoptosis is a major secondary injury factor, we further investigated whether Mn@CDs could reduce ROS-induced apoptosis *in vitro*. The flow cytometry data (Fig. 5h and Supplementary Fig. 22) revealed that the Mn@CDs significantly reduced the H_2O_2-induced apoptosis rate in the NSC-34 cells from 27.18% to 5.62%, and in the SH-SY5Y cells from 55.12% to 5.02%. These findings suggest that Mn@CDs effectively reduce ROS levels and preserve mitochondrial function in neuronal cells.

Enhanced motor function and extended lifespan of SOD1 mice with Mn@CDs

Given the cytoprotective effects of Mn@CDs in the cell models, we used SOD1-G93A transgenic ($SOD1^{G93A-Tg}$) mice as an animal model to further assess the effects of Mn@CDs (Fig. 6a)[53]. First, we investigated the pharmacokinetics of Mn@CDs. As shown in Supplementary Fig. 23, Mn@CDs exhibited a half-life of 1.426 h after intravenous injection, suggesting that they could be rapidly cleared from the blood and distributed into the organs. Subsequently, we analyzed the biodistribution of the Mn@CDs in the $SOD1^{G93A-Tg}$ mice. At 2 h postinjection, the Mn@CDs were primarily localized in the liver and kidney, with smaller amounts detected in other organs. However, at 12 hours postinjection, their accumulation in metabolic organs decreased, whereas their accumulation increased in the spinal cord, which is a critical site of oxidative damage in individuals with ALS (Fig. 6b). The accumulation of Mn@CDs in the spinal cord could be attributed to the passive diffusion effect resulting from its small size and the enhanced blood-spinal cord barrier and blood-brain barrier permeability caused by oxidative damage in the ALS progression[54–56]. Moreover, Mn@CDs could also accumulate in skeletal muscle, which ensures their protection on the neuromuscular junction (NMJ), thereby enhancing skeletal muscle motor function. From 24 h to 48 h, Mn@CDs could be majorly cleared via renal excretion and eliminated from the body through urine (Fig. 6b and Supplementary Fig. 24).

Edaravone, a marketed drug for the treatment of ALS, works through a free radical scavenging mechanism, which aligns with the design concept of Mn@CDs. Therefore, we used Eda as a positive control drug to assess the therapeutic efficacy of the Mn@CDs. Here, we administered Eda at an optimal dosage of 15 mg/kg once daily[57,58], while Mn@CDs were dosed at 2.5 mg/kg twice weekly. First, we evaluated the protective effect of the Mn@CDs on the mobility of model mice. In the rotarod test, no

significant differences in motor performance were observed between the treated and untreated mice during the early stages of the study. Over time, SOD1$^{G93A-Tg}$ mice treated with Eda presented a slower decline in rotarod performance than SOD1$^{G93A-Tg}$ mice treated with PBS did, while the rotarod performance of Mn@CD-treated group was even better than that of Eda (Fig. 6c). Additionally, we used a 5-minute open field test to assess the overall muscle strength and balance of the mice. As shown in Fig. 6d-f, the activity of the Mn@CD-treated SOD1$^{G93A-Tg}$ mice were markedly greater than that of the PBS-treated mice in terms of the number of rearing episodes and total distance traveled. Notably, the Mn@CD-treated SOD1$^{G93A-Tg}$ mice exhibited a movement pattern more similar to that of WT mice, frequently crossing the center of the cage, whereas the PBS-treated SOD1$^{G93A-Tg}$ mice predominantly stayed near the cage walls starting at week 17. Compared with that of WT mice, the weight of SOD1$^{G93A-Tg}$ mice was significantly decreased, and Mn@CDs treatment slowed this process, although the difference was not statistically significant (Fig. 6g). More importantly, the survival of the Mn@CD-treated mice was longer than that of the model group (Fig. 6h). The average survival of the SOD1$^{G93A-Tg}$ model group was 160 days, while Mn@CD treatment extended the average survival to 174.5 days, which is a 93% improvement over the effect of Eda treatment (167.5 days). In addition, the *in vivo* chronic toxicity of the Mn@CDs has been evaluated. It has been confirmed that the 69 days of Mn@CDs administration did not cause Mn accumulation in any of the major tissues (Supplementary Fig. 26) or abnormal alterations in major organs (Supplementary Fig. 27), body weight (Supplementary Fig. 28), blood routine indexes (Supplementary Fig. 29), and blood biochemical indicators (Supplementary Fig. 30).

Neuroprotection and preservation of motor units with Mn@CDs in SOD1 mice

We next investigated how Mn@CD treatment affected the maintenance of spinal motor neurons, neuromuscular junctions, and muscle volume at late time points during disease progression. Cohorts from each group were euthanized at 150 days of age. Motor neurons in the ventral horn of the lumbar spinal cord were visualized via Nissl staining. As expected, the number of motor neurons progressively decreased over time in the transgenic mice compared with the WT mice. However, compared with those in the PBS group, the number of motor neurons in the SOD1$^{G93A-Tg}$ group treated with Mn@CDs was significantly greater (Fig. 7a). Similarly, via Western blot analysis, variations in the expression of the neuronal marker choline acetyltransferase (ChAT) across the different groups exhibited a consistent trend (Fig. 7b). These results indicated that treatment with Mn@CDs prevented the deterioration of spinal motor neurons in the ALS model mice. Defects in NMJs are a hallmark of ALS[59]. Therefore, we examined the integrity of NMJs and the extent of muscle innervation. Compared with those in the WT group, the percentage of innervated NMJs in the SOD1$^{G93A-Tg}$ mice significantly decreased at 150 days (Fig. 7c), whereas the Mn@CD-treated group presented significantly more intact NMJs than did the PBS group. These results indicate that Mn@CD treatment helps SOD1$^{G93A-Tg}$ mice maintain muscle

innervation for a longer period, which is consistent with improved performance in the rotarod test and the open field test.

Since NMJ defects are considered one of the causes of muscle atrophy in ALS[60], we measured the weights of the gastrocnemius muscles in the mice and normalized them to body weight. As expected, the average weights of these muscles were significantly lower in the SOD1$^{G93A-Tg}$ mice than in the WT mice, while Mn@CD treatment significantly alleviated this decrease (Fig. 7d). We subsequently evaluated the effect of Mn@CD treatment on muscle fiber size. Analysis of the size distribution of fiber cross-sectional areas (CSAs) in the gastrocnemius showed that, compared with PBS-treated SOD1$^{G93A-Tg}$ mice, Mn@CD treatment significantly increased the cumulative percentage and mean value of CSA in SOD1$^{G93A-Tg}$ mice (Fig. 7e-g), indicating a beneficial effect of Mn@CD treatment on muscle atrophy.

Spinal cord gliosis is a prominent pathological feature in both ALS patients and rodent models[61], as excessive activation of astrocytes and microglia has been shown to drive late-stage disease progression[62]. Therefore, we assessed microglial activation through GFAP and Iba-1 immunohistochemistry in spinal cord sections. The analysis revealed a significant increase in both the GFAP and Iba-1 signals in the SOD1$^{G93A-Tg}$ mice compared with those in the WT controls, which was attenuated following Mn@CD treatment (Fig. 7h). Consistently, Western blot analysis further confirmed that Mn@CD treatment effectively reduced the expression levels of GFAP and Iba-1 in the spinal cord (Fig. 7i). These findings indicate that Mn@CDs improve neuroglial proliferation in microglia and astrocytes in SOD1$^{G93A-Tg}$ mice, alleviating neuroinflammation.

In vivo antioxidant activity and mitochondrial homeostasis maintenance by Mn@CDs

RNA-seq was performed on mouse spinal cord tissues to elucidate the therapeutic mechanism of Mn@CDs in ALS. Differences in gene expression levels among the WT, SOD1$^{G93A-Tg}$ + PBS, SOD1$^{G93A-Tg}$ + Eda, and SOD1$^{G93A-Tg}$ + Mn@CD groups are shown as fragments per kilobase of exon model per million mapped fragments. Volcano plots (Fig. 8a) revealed that, compared with the PBS group, the Mn@CD group had 474 upregulated genes and 104 downregulated genes. Next, a more detailed comparison of the transcriptional levels in the WT group revealed that 633 genes were restored to near-normal levels after Mn@CD treatment (Fig. 8b). Functional pathway enrichment analysis (using the Kyoto Encyclopedia of Genes and Genomes [KEGG]) revealed that the genes normalized by Mn@CD treatment were strongly associated with ALS and pathways related to multiple neurodegenerative diseases (Fig. 8c), which suggests that Mn@CD therapy is effective. The normalized heatmap revealed a significant reduction in the number of ROS-related genes in the spinal cord tissues of SOD1$^{G93A-Tg}$ mice following Mn@CD treatment (Fig. 8d). Furthermore, to clarify the underlying therapeutic mechanisms, the screened differentially expressed genes (DEGs) were subjected to clustering and enrichment analyses. Using the Gene Ontology (GO) database, functional clustering analysis was performed with -log10 (*P* value) as the evaluation criterion. The findings indicated that multiple mitochondrial function-related pathways being significantly enriched (Fig. 8e). It has been reported that oxidative stress and

mitochondrial degeneration are positively correlated with the pathological progression of ALS. These findings suggest that Mn@CDs could slow disease progression in ALS mice by reducing ROS levels and improving mitochondrial function.

Nrf2 is a key transcription factor that regulates cellular antioxidant responses[63]. Western blot analysis was performed to detect the protein expression of Nrf2 target genes, including heme oxygenase-1 (HO-1), NAD(P)H quinone oxidoreductase 1 (NQO1), glutamate-cysteine ligase catalytic subunit (GCLC), and glutamate-cysteine ligase modifier subunit (GCLM), in the lumbar spinal cord of mice. The results showed that Mn@CD treatment upregulated the expression of antioxidant genes, indicating that the Nrf2 antioxidant signaling pathway was activated by Mn@CDs, which may have contributed to their neuroprotective effects (Fig. 8f).

To elucidate the molecular basis of the protection effect of Mn@CDs on mitochondrial function, we focused on the activity of mitochondrial respiratory chain complex I since the related pathways were highly enriched in Fig. 8e. Moreover, the dysfunction of not only complex I but also complex II was reported in ALS progression[64]. In light of this, the activities of these two complexes were examined in the spinal cord of $SOD1^{G93A-Tg}$ mice. As shown in Fig. 8g, we confirmed that the activities of complexes I and II were markedly rescued after Mn@CD treatment. Correspondingly, the decline of NDUFB8 (the marker of mitochondrial complex I) and SDHB (the marker of mitochondrial complex II) was also significantly ameliorated, while other Nrf2 signaling pathway-related proteins were upregulated (Fig. 8h), indicating activation of the cellular antioxidant defense system. Benefited from the recovery of activity, the morphology and quantity of mitochondria were expected to be rescued. TEM was subsequently performed to visualize mitochondria from the anterior horn of the lumbar spinal cord from Mn@CD- or PBS-treated $SOD1^{G93A-Tg}$ mice. As shown in Fig. 8i, compared with WT mice, symptomatic $SOD1^{G93A-Tg}$ mice presented mitochondrial abnormalities, including vacuolization, cristae disruption, and double-membrane rupture. In contrast, in the ventral horn of the spinal cord treated with the Mn@CDs, the number of abnormal mitochondria was reduced, with the majority of the mitochondrial cristae forming compact tubules in an orderly manner. Furthermore, mtDNA content has previously been used as an indicator of mitochondrial quantity in various diseases, including the significant reduction observed in the spinal cord of ALS patients[65]. To assess mitochondrial quantity, we measured the transcriptional levels of several mitochondrial genes as surrogate markers and found that mtDNA levels in the spinal cords of $SOD1^{G93A-Tg}$ mice were significantly lower than those in the spinal cords of WT mice. Continuous Mn@CD treatment improved these levels (Fig. 8j and Supplementary Fig. 31). These findings suggest that Mn@CDs play a protective role in mitochondrial respiratory chain complexes, thereby modulating mitochondrial structure and quantity.

Discussion

Approximately 150 years ago since the initial definition of ALS, clinical treatment options for this disease remain extremely limited. Therefore, developing novel therapeutics that enhance the efficacy of existing

clinical medications is of significant importance for advancing the current state of ALS treatment research. Given the significant role of oxidative stress in the pathogenesis of ALS, nanozyme-based antioxidant therapy—owing to its superior ROS scavenging capability—presents a promising therapeutic strategy.

In this work, we developed Mn@CDs, in which Mn exists as single atoms within the CD scaffold, potentially mimicking the active center and metallocofactor of natural enzymes. We revealed that Mn doping could significantly alter the structure and functional group composition of CDs. UV-vis and ^{1}H-NMR confirmed that Mn doping reduced the proportion of enol structures in CDs while increasing the proportion of ketone structures; FT-IR spectra of CDs and Mn@CDs indicated that the introduction of Mn promoted an increase in the content of amide structures in CDs. XPS results further demonstrated that Mn ions in Mn@CDs not only coordinated with containing O/N functional groups, but also that a portion of Mn^{2+} transferred electrons to the empty π orbitals of C = O, C = N, or pyrrole groups while coordinating with these groups, forming backdonation π bonds. This electron transfer effect not only resulted in the coexistence of Mn^{2+} and Mn^{3+} in Mn@CDs, but also significantly altered the surface structure and local coordination geometry of CDs. XAFS and XRD results collectively confirmed that Mn was dispersed as single atoms in the CDs scaffold; specifically, XAFS data further clarified that Mn ions in Mn@CDs mainly formed coordination structures with 4–5 N/O atoms. The coordination of single-atom Mn with N and O modulates the overall structure of CDs, which facilitates electron transfer and binding with superoxide anions in Mn@CDs, ultimately endowing the nanozymes with a remarkably high activity of over 7×10^{4} U/mg.

Theoretical calculations from both kinetic and thermodynamic perspectives further establish a clear structure–activity relationship, identifying a MnN_2O_2 motif with amide-derived N atoms as the most plausible active center. This site satisfies the SOD selectivity criterion, indicating that it can efficiently activate $O_2^{\bullet-}$ while avoiding over-strong binding of reactive intermediates. Differential charge density and Bader charge analyses reveal that Mn in this environment remains positively charged and donates electron density to the surrounding N/O ligands and carbon framework, forming strongly covalent Mn–N/O–C interactions that tune the Mn d-band center to an optimal range for SOD-like catalysis. Moreover, its non-planar geometry closely resembles the three-dimensional coordination environment of natural MnSOD, suggesting that both the local electronic structure and the enzyme-like spatial arrangement are crucial for achieving the exceptional activity and selectivity of Mn@CDs.

This outstanding antioxidant enzyme-like activity endows Mn@CDs with the ability to protect motor neurons from ROS-induced damage at the cellular level. Moreover, under oxidative stress, Mn@CDs entered cells and mitochondria more effectively, probably due to increased cellular and mitochondrial membrane permeability resulting from oxidative damage. This property endows Mn@CDs with potential for mitochondrial protection.

More importantly, the results from the ALS animal model demonstrated that Mn@CDs exerted a superior therapeutic effect compared to edaravone, a clinically approved drug used for antioxidant therapy, as

evidenced by the prolonged survival as well as the delay of motor neuron degeneration, NMJ denervation, muscle unit atrophy, and gliosis. There might be some potential explanations for this enhanced efficacy. First, as a small-molecule compound, edaravone is cleared from the body more rapidly following administration[58], which could limit its duration of action. In addition, our findings showed that Mn@CD therapy activated the Nrf2 signaling pathway, which is consistent with the observations using nanozymes or drug molecules with antioxidant or anti-inflammatory effects to treat neurological diseases[66,67]. This phenomenon probably further enhanced the endogenous cellular antioxidant activity. However, the precise mechanism underlying Mn@CD-mediated activation of Nrf2 signaling pathway remains to be further elucidated.

Transcriptomic analysis further revealed that Mn@CDs successfully inhibited the activation of ROS-related pathways and restored the expression of mitochondrial function-related pathways after treatment. According to our data, Mn@CDs reinstated the activities of mitochondrial respiratory chain complexes I and II. It is well known that the dysfunction mechanism of mitochondrial complexes is highly related to the increased ROS level in ALS. Once the activity of the mitochondrial complexes is impaired, ROS are further generated, leading to the formation of a vicious cycle[68]. Given this, breaking this vicious cycle is crucial for maintaining mitochondrial quantity and quality, thereby exerting pronounced effect on ALS treatment. Intriguingly, the genes normalized by Mn@CD treatment in our KEGG functional pathway enrichment analysis are associated with not only ALS, but also neurodegenerative diseases like Alzheimer disease and Parkinson disease. This suggests that Mn@CDs may exert a broad-spectrum therapeutic effect across several neurodegenerative diseases.

In summary, our study provides a promising platform for nanozyme-based antioxidant therapy and broadens the applications of nanozymes in ALS treatment. In the future, a key challenge for Mn@CD is to ensure the large-scale mass-production, thereby pushing forward its preclinical-to-clinical translation in medical fields.

Methods

Synthesis of Mn@CDs

First, 2.1 g of glutathione and 100 mg of manganese (II) perchlorate hexahydrate were dissolved in 70 mL of formamide. The mixture reacted in an autoclave for 8 h at 160°C. The resulting mixture was centrifuged at 3000 rpm for 10 min to remove the precipitate. The resulting supernatant was subsequently dialyzed with a 3500 Da dialysis bag for 5–7 days. For further purification, the solution containing Mn@CDs was frozen at -80°C for 1 h and then thawed at room temperature. The solution was filtered multiple times via a 0.22 μm filter to remove the precipitate during thawing; this method was typically performed 4–5 times. Finally, the Mn@CD powder was prepared via vacuum freeze-drying.

SOD-like activity assay

The SOD-like activity of the Mn@CDs was determined by using a Total Superoxide Dismutase Assay Kit (Dojindo, S311-10). The experimental procedure strictly adhered to the manufacturer's instructions, and the SOD-like activity was evaluated by measuring the inhibition of the WST-1 reaction at various concentrations of Mn@CDs. The absorbance was measured at 450 nm via an S1LFA-SN microplate reader (Agilent Biotek, USA).

Scavenging superoxide anion

A mixture was prepared by combining 20 μL of 10 mM xanthine, 20 μL of 1 U/mL xanthine oxidase, and 10 μL of 200 mM 5-tert-butoxycarbonyl 5-methyl-1-pyrroline N-oxide (BMPO) with either 50 μL of PBS buffer or Mn@CDs (final concentrations of 50, 100, and 200 μg/mL). The resulting mixture was incubated at room temperature for 10 min before ESR measurements.

Scavenging hydroxyl radicals

100 μL of $FeSO_4$ (5 mg/ml) was mixed with 10 μL of 5,5-dimethyl-1-pyrroline N-oxide (DMPO) and 80 μL of deionized water or 80 μL of various concentrations of Mn@CDs (final concentrations: 50, 100, and 200 μg/mL). Then, 10 μL of 30% H_2O_2 was added, and the mixture was stirred for 5 min before ESR measurements.

Instrumentation for characterization of Mn@CDs

UV-vis absorption spectra were recorded using a Lambda 1050 + Ultraviolet spectrometer (PerkinElmer, USA). Fluorescence spectra were measured with an FL 8500 Fluorescence spectrometer (PerkinElmer, USA). XPS spectra were acquired using a Thermo Escalab 250Xi (Thermo Fisher Scientific, USA). ^{1}H-NMR spectra were recorded on an Agilent DD2 600 MHz spectrometer (room temperature, D_2O as the solvent, CDs with final concentration of 2 mg/mL). FT-IR spectra were obtained using a Bruker INVENIO-S spectrometer (Bruker, Germany). Spherical aberration-corrected transmission electron microscope (AC-TEM) images and TEM images were captured using a FEI Themis Z (Thermo Fisher Scientific, USA) and a FEI Tecnai G2 F30 (FEI, USA) at an acceleration voltage of 300 kV, respectively. XRD data and ESR spectra were collected by using a Bruker D8 ADVANCE (Germany) with a scan rate of 6 ° / min and a Bruker A300-9.5/12 (Switzerland) at room temperature, respectively. The XAFS spectra were recorded with the specific detectors in the beamline 1W1B of Beijing Synchrotron Radiation Facility (BSRF), China. Transmission mode was adopted to collect the XAFS for the reference samples of Mn and the Mn @CDs. XAFS data were normalized and analyzed with least-squares fitting (LSF) to fit the spectra and to calculate the coordination structure for Mn using the IFEFFIT Athena software (CARS, the Consortium for Advanced Radiation Sources at University of Chicago, IL, USA).

Computational method

Geometry optimizations and energy calculations were carried out using the Perdew–Burke–Ernzerhof (PBE) functional within the generalized gradient approximation, with van der Waals interactions accounted for by the DFT-D3BJ method[69–71]. A cut-off energy of 500 eV and Gaussian smearing at 0.05 eV were applied to improve the accuracy of the computations. Brillouin zone sampling was performed using Monkhorst–Pack k-point meshes of (3 × 3 × 1) for geometry optimization and (5 × 5 × 1) for DOS calculations. Convergence criteria were set at 10^{-5} eV for electronic structure and 0.02 eV $Å^{-1}$ for ionic forces. All simulations were executed using the VASP package, with the projector-augmented wave (PAW) method for pseudopotential generation[72–74]. All the calculations were performed using the Vienna Ab initio Simulation Package (VASP)[75,76].

Cell culture

SH-SY5Y cells were obtained from the American Type Culture Collection and were cultured in DMEM-F12 supplemented with 10% FBS supplemented with 1% penicillin–streptomycin. NSC-34 cells were obtained from Hongshun Biotechnology Co., Ltd. (Shanghai, China) and were cultured in DMEM supplemented with 10% FBS supplemented with 1% penicillin–streptomycin. All the cells were cultured at 37°C in an atmosphere with 5% CO_2, and the culture media were replaced every 2 days.

Cellular ROS generation assay

For $O_2^{\bullet-}$ and ROS detection via flow cytometry, the cells were seeded in 12-well plates overnight (30,000 cells per well for NSC-34 cells and 20,000 cells per well for SH-SY5Y cells). The cells were preincubated with Mn@CDs (20 μg/mL) for 2 h and subsequently stained with DHE (Biorigin, BN27103), DCFH-DA (Dojindo, R253), or MitoSOX Green (Thermo, M36006) following the manufacturer's protocols. After that, the cells were stimulated with PQ (Sigma, 856177) (40 μM for NSC-34 cells and 250 μM for SH-SY5Y cells) for 24 h or stimulated with H_2O_2 (400 μM) for 4 h. After treatment, the cells were washed with PBS, collected, and analyzed with a FACS Calibur (BD Biosciences, USA). At least 10,000 cells were analyzed, and the intensity of the fluorescence signal was processed with FlowJo_V10.

To evaluate the intracellular ROS levels via confocal microscopy, the cells were plated in glass bottom cell culture dishes for 48 h (20,000 cells per dish for NSC-34 cells and 10,000 cells per dish for SH-SY5Y cells). The cells were then pretreated with Mn@CDs (20 μg/mL) for 2 h, stained with DCFH-DA (Dojindo, R253) according to the manufacturer's protocol, and stimulated with H_2O_2 (400 μM) for 4 h. Subsequently, the cells were washed with PBS, and a laser scanning confocal microscope (ZIESS, LSM980, Germany) was used to capture the images. ImageJ (v1.52) was utilized for the quantification of the fluorescence signal.

Intracellular uptake evaluation

NSC-34 cells were seeded in 100 mm dishes overnight followed by stimulation with H_2O_2 (400 μM) for 4 h. Subsequently, the cells were treated with Mn@CDs (20 μg/mL) for 12 h. Subsequently, the cells were digested with HNO_3 and H_2O_2 at 130°C and brought up to a volume of 10 mL with ddH_2O. The Mn content was detected via ICP—MS (PE, NEXION1000, USA) and was normalized to the number of cells.

Mitochondrial colocalization

NSC-34 cells were plated in glass bottom cell culture dishes (20,000 cells per dish) for 48 h. The cells were stimulated with H_2O_2 (400 μM) for 4 h and incubated with FITC-labeled Mn@CDs (20 μg/mL) for 12 h. Afterwards, MitoTracker Red CMXRos (Beyotime, C1049B) was used for the staining of mitochondria, and Hoechst 33342 (Beyotime, C1027) was used for the staining of nuclei. Images were captured via a laser scanning confocal microscope (Zeiss, LSM980, Germany). ImageJ (vl.52) was used to quantify Pearson's coefficient.

Cell apoptosis analysis

The cells (30,000 cells per well for the NSC-34 cells and 20,000 cells per well for the SH-SY5Y cells) were seeded in 12-well plates overnight. After preincubation with Mn@CDs (20 μg/mL) for 2 h, the cells were treated with H_2O_2 (400 μM) for 12 h (for NSC-34 cells) or 8 h (for SH-SY5Y cells). The cells were subsequently collected and resuspended in Annexin V binding solution and stained with Annexin V-FITC and propidium iodide (PI) (Dojindo, AD10) for 15 min at room temperature. After staining, the cells were washed and resuspended in Annexin V binding solution until detection via a FACSCalibur. At least 10,000 cells were analyzed, and the data were processed with FlowJo_V10.

Mitochondrial membrane potential determination

The cells were plated in glass bottom cell culture dishes for 48 h (20,000 cells per dish for NSC-34 cells). The cells were subsequently preincubated with Mn@CDs (20 μg/mL) for 2 h, stimulated with H_2O_2 (400 μM) for 4 h, and stained with TMRM (Thermo, I34361) following the manufacturer’s protocol. After washing with PBS, a laser scanning confocal microscope (Olympus, FV3000, Japan) was used to capture the images. ImageJ (v1.52) was utilized for the quantification of the fluorescence signal.

Cellular Ca^{2+} concentration detection

The cells (30,000 cells per well for NSC-34 cells) were seeded in 12-well plates overnight, followed by pretreatment with Mn@CDs (20 μg/mL) for 2 h. Subsequently, the cells were incubated with H_2O_2 (400

μM) for 4 h. Fluo-4 AM (Thermo, F14217) was utilized for staining, and a FACS Calibur was used for detection. FlowJo_V10 was used for data analysis of at least 10,000 cells.

Animals

Male hemizygous SOD1$^{G93A-Tg}$ mice [B6. CgTg(SOD1*G93A)1Gur/J] (stock no. 004435) were purchased from the Jackson Laboratory (Maine, USA) and bred with female wild-type C57BL/6J mice to continue the species. Polymerase chain reaction (PCR) was conducted for genotyping neonatal mice according to the guidelines of the Jackson Laboratory (https://www.jax.org/strain/004435). The littermates with a nontransgenic genotype were regarded as wild-type healthy controls. All the animals were raised under controlled housing conditions with free access to food and water under a 12 h light–dark cycle. All animal studies were performed according to the protocol approved by the Institutional Animal Care and Use Committee at the Institute of Biophysics, Chinese Academy of Sciences (SYXK2023177).

Drug administration

The mice were randomly divided into four groups: (1) the wild-type healthy group, which was administered PBS; (2) the SOD1$^{G93A-Tg}$ model group, which was administered PBS; (3) the SOD1$^{G93A-Tg}$ model group, which was administered Mn@CDs; and (4) the SOD1$^{G93A-Tg}$ model group, which was administered Eda (Solarbio, IE0020). Mn@CDs (or an equal volume of PBS) was administered via intravenous injection at a dosage of 2.5 mg/kg twice a week, which was based on the metabolic profile of Mn@CDs (as exhibited in Fig. 6b, Supplementary Fig. 23, and Supplementary Fig. 24) and the pre-experiment evaluating the therapeutic effects of Mn@CDs at different concentration gradients of administration doses (as shown in Supplementary Fig. 25). Eda was intraperitoneally injected at an optimal dosage of 15 mg/kg once a day according to the literature[55,56]. The drug was administered from the onset (14 weeks of age) to the end stage (23 weeks of age) of disease.

Behavioral analysis

To evaluate the coordination, muscle strength, and endurance of the mice, a rotarod test was performed once per week starting from 14 to 21 weeks of age (10 mice for each group). The mice were trained for one week prior to the start of the experiment. In the formal test, the latency to fall from the rotarod (SansBio, SA102, China) of each mouse was examined as the speed of the rotating cylinder increased from 0 to 40 rpm in 4 min. The best time of the three trials was recorded.

An open field test was conducted to assess overall locomotor activity at 14, 17, and 21 weeks of age. The mice were allowed to adapt to the environment of the apparatus, which was a square arena with an infrared detector (SansBio, SA215S, China), for one week prior to the formal test. Each mouse was gently

placed into a corner of the arena. The total distance traveled and the number of rearing episodes were recorded for 5 min via a video camera.

During the treatment process, the weight of each mouse was measured every two days.

Survival assay

The mortality of the mice was defined as the inability to right themselves 30 sec after being placed on one side. The age at which each mouse met the death criterion was recorded in days, and the survival assay was performed by Kaplan–Meier analysis.

Histology evaluation

At the late time point of disease (150 days of age), the mice were anesthetized, sacrificed and transcardially perfused with saline followed by 4% PFA (5 mice in each group). The indicated tissues were isolated and postfixed in 4% PFA for at least 24 h. The tissues were then paraffin-embedded and sliced.

For Nissl staining, the sections from the lumbar spinal cord were dewaxed, hydrated, and immersed in cresyl violet staining solution. After that, the sections were dehydrated, sealed with neutral gum, and imaged using a slide scanner (Aperio CS2, Leica Biosystems, Germany). Motor neurons in the ventral horn with a minimum diameter of 20 μm were quantified by ImageJ (v1.52)[77].

For NMJ immunofluorescence staining, the sections from the gastrocnemius muscle were dewaxed, followed by dehydration, antigen repair, and serum blocking. The sections were then incubated with anti-synaptic vesicle protein 2 antibody (DSHB, SV2) and anti-neurofilament antibody (Sigma, SAB4200740). Subsequently, Alexa 488-labeled secondary antibody (Thermo Scientific, A11001). After that, the sections were stained with α-Bungarotoxin-tetramethylrhodamine (Sigma, T0195) and sealed. Images were captured with a laser scanning confocal microscope (Zeiss, LSM980, Germany).

For muscle weighting, the masses of isolated gastrocnemius muscles from both the left and right sides were recorded before fixation and embedding. During data processing, the mass of muscle was normalized to the body weight of each mouse.

For H&E staining, the sections from the gastrocnemius muscle were dewaxed, dehydrated, stained with hematoxylin and eosin, dehydrated, and sealed. Images of the slides were acquired with an Aperio CS2 slide scanner. The CSA of the gastrocnemius muscle fibers was determined via ImageJ (v1.52).

For immunohistochemistry, sections from the lumbar spinal cord were dewaxed and hydrated. Tris-EDTA buffer (pH 8.0) was used for high-pressure antigen retrieval. After blocking with 5% goat serum, the sections were incubated overnight at 4°C with different antibodies, including anti-GFAP antibody

(Servicebio, GB11096), anti-Iba1 antibody (Servicebio, GB12105). The sections were subsequently incubated with HRP-conjugated goat anti-mouse secondary antibody (ZSBG-BIO, PV-6002) or HRP-conjugated goat anti-rabbit secondary antibody (ZSBG-BIO, PV-6001) for 20 min at 37°C. After being stained with diaminobenzidine (ZSBG-BIO, ZLI-9019) and hematoxylin (ZSBG-BIO, ZLI-9610), the sections were sealed, and an Aperio CS2 slide scanner was used to acquire images.

Immunoblotting

The lumbar spinal cord of each mouse was collected. RIPA lysis buffer (Beyotime, P1003B) supplemented with protease inhibitor cocktail (Sigma, 04693132001) and phosphatase inhibitor cocktail (Beyotime, P1081) was used to prepare tissue lysates, which were subsequently homogenized through a tissue homogenizer. The protein concentration was determined via the use of the BCA reagent (Thermo Scientific, 23228). The proteins were subsequently boiled with SDS loading buffer (Genstar, E153), separated on 10–15% SDS—PAGE gels, and transferred to polyvinylidene difluoride membranes. The membranes were subsequently blocked with nonfat milk (5% in PBS) and incubated with the following primary antibodies: anti-ChAT antibody (Proteintech, 20747-1-AP), anti-GFAP antibody (CST, 12389), anti-Iba1 antibody (CST, 17198), anti-Nrf2 antibody (CST, 12721), anti-HO-1 antibody (Proteintech, 10701-1-AP), anti-NQO1 antibody (Santa Cruz, sc-376023), anti-GCLC antibody (Santa Cruz, sc-166356), anti-GCLM antibody (Santa Cruz, sc-55586), anti-NDUFB8 antibody (Proteintech, 14794-1-AP), anti-SDHB antibody (Proteintech, 10620-1-AP), and anti-actin antibody (ABclonal, AC004). After that, the membranes were incubated with an HRP-conjugated goat anti-rabbit IgG (H + L) secondary antibody (Emarbio, EM35111) or an HRP-conjugated goat anti-mouse IgG (H + L) secondary antibody (Emarbio, EM35110) at room temperature for 1 h. The images were detected with an enhanced chemiluminescence (ECL) system (Touch imager, E-blot, China).

RNA-seq

The lumbar spinal cord of each mouse was collected and homogenized through a tissue homogenizer. TRIzol™ reagent (Thermo Scientific, 15596026) was subsequently used to extract total RNA from each sample according to the manufacturer's instructions. After sequencing, raw data in fastq format were first processed to clean data by removing reads containing adapters via Cutadapt (v4.4)[78]. The clean reads were mapped to the GRCm38 genome via HISAT2 (v2.2.1) with the default parameters[79]. Prior to differential gene expression analysis, the read counts were adjusted by the edgeR program package through one scaling normalized factor[80], and the threshold *P* value was 0.05 with a fold change ≥ 1.5. A volcano plot of the differentially expressed genes was generated via the R ggplot2 package (v3.3.5). Heatmaps of differentially expressed genes were generated via TBtools (v2.112)[81]. KEGG and GO enrichment analyses were conducted via DAVID[82], and all KEGG and GO terms were visualized via the R ggplot2 package.

Mitochondrial complex activity detection

The lumbar spinal cord of each mouse was obtained and the activities of mitochondrial complexes I and II were detected using the commercial assay kits (Abbkine, KTB1850 and KTB1860) and a SpectraMax Plus microplate reader (Molecular Devices, USA) following the manufacturer's instructions. The relative activity was calculated and normalized to the data of WT group.

Real-time quantitative PCR (RT—qPCR)

After excision and homogenization of the lumbar spinal cord of each mouse total RNA was extracted via TRIzol™ reagent. 5×All-in-one-RT MasterMix (Abm, G490) was used to generate cDNA. The cDNA from each sample was subsequently subjected to RT—qPCR via Taq Pro Universal SYBR qPCR Master Mix (Vazyme Biotech, Q712) on a QuantStudio™ 7 Flex system (Thermo Scientific, USA) with the primers shown in Supplementary Table 5. QuantStudio™ Real-Time PCR software was used to record and analyze the relative mRNA expression levels via the $2^{-\Delta\Delta CT}$ method.

Bio-TEM

The lumbar spinal cords per group were collected and fixed with 2.5% glutaraldehyde fixation solution (Novon, SS0561). The samples were subsequently washed and further fixed with 1% osmic acid. Following dehydration with gradient ethanol, the samples were infiltrated with acetone and resin and finally embedded with pure resin for polymerization. The samples were subsequently cut via an ultramicrotome (Leica, EM UC7, Germany) to obtain sections with thicknesses of 70–80 nm, which were subsequently stained with uranyl acetate for 15 min and lead citrate for 5 min. The images were obtained via transmission electron microscope (FEI, Spirit, USA) at 120 kV.

Biodistribution and pharmacokinetics study

$SOD1^{G93A-Tg}$ mice were intravenously injected with Mn@CDs (2.5 mg/kg) or an equal volume of PBS. For biodistribution study, at 2, 12, 24, and 48 h, the mice were anesthetized and sacrificed. The spinal cord, heart, liver, spleen, lung, kidney, brain, and gastrocnemius muscle were obtained, digested with HNO_3 and H_2O_2 at 130°C. For pharmacokinetics study, 20 μL of blood was collected from each mouse by tail clipping at 0, 0.25, 0.5, 1, 2, 4, 7, 17, and 24 h. The blood samples were digested with HNO_3 and H_2O_2 at 130°C. Urine and feces were collected using metabolic cages at 12, 24, 36, and 48 h. The urine and feces samples were digested with HNO_3 and H_2O_2 at 130°C. The content of Mn was detected via ICP—MS (PE, NEXION1000, USA). The relative concentrations of Mn@CDs in the organs were normalized to that of the PBS group. The contents of Mn@CDs excreted in the urine and feces were expressed as percentages of total injected dose Mn@CDs. The mice were fed with Mn-free chow diet (Jiangsu Xietong Pharmaceutical Bio-Engineering Co.,Ltd.) before the experiments.

Toxicity evaluation in vivo

WT C57BL6/J mice were utilized to examine the toxicity of the Mn@CDs *in vivo*. The experimental conditions in terms of the mode and dose of administration as well as the start and end times of administration were replicated to align with those employed in the behavioral analysis. The body weight of each mouse was monitored every two days. After treatment, the mice were anesthetized and sacrificed. The neural tissues (spinal cord and brain) were obtained for ICP-MS analysis to evaluate Mn accumulation. The main organs (heart, spleen, lung, liver, kidney, and brain) were obtained for H&E staining and pathological analysis. Blood samples, including white blood cells (WBCs), red blood cells (RBCs), hemoglobin (HGB), platelets (PLTs), lymphocytes (Lymph), monocytes (Mon), and granulocytes (Gran), were collected for routine blood tests. The serum, including alanine aminotransferase (ALT), aspartate transaminase (AST), creatinine (CREA), urea (UA), creatine kinase (CK), and lactate dehydrogenase (LDH), was separated for blood biochemical analysis.

Statistical analysis

All the quantitative data are presented as the means ± SDs. Unpaired two-tailed Student's t tests were used to evaluate significant differences between two groups with one variable. One-way ANOVA with Tukey's multiple-comparison test was used to evaluate significant differences for more than two groups with one variable. Repeated-measures ANOVA with a post hoc least significant difference (LSD) test was used to evaluate significant differences in rotarod latency, open field total distance, rearing episodes, and body weight changes. Kaplan—Meier analysis with the log-rank test was used to evaluate significant differences in survival curves. A *P* value less than 0.05 was considered significant.

Declarations

Competing Interests Statement

The authors declare no competing interests.

Author contribution Statement

K.F. conceived and designed the whole project. Y.H. designed and performed the experiments. J.L., Q.X., W.Y. and D.L. designed and synthesized the Mn@CDs. X.G. contributed to the theoretical modeling of Mn@CDs. Y.H., G.T. designed and purified the animal experiments. Y.H., Q.W. contributed to RNA-seq analysis. R.X. contributed to the schematic diagram. L.W., Y.R. contributed to the analysis of synchrotron radiation. K.F., Y.H., C.L., Q.L and X.G. wrote the manuscript with input from all authors.

Acknowledgments

This work was financially supported by the Fundamental Research Funds for the Central Universities (2024IAIS-QN001), the National Natural Science Foundation of China (32171392; 22467013, 32371469, 32350410425), the Youth Innovation Promotion Association of the Chinese Academy of Sciences (Y2023024), the Gan Poyang Talents Support Program, the Academic and Technical Leaders of Major Disciplines (20232BCJ23014) and the Key Laboratory of Biomacromolecules, Chinese Academy of Sciences (ZGD-2023-03), Innovative Projects of Regular Universities of Guangdong Province (2024KTSCX049), Directional Institutionalized Scientific Research Platform relies on Beijing Synchrotron Radiation Facility of the Chinese Academy of Sciences. We thank Xing Jia and Qing Bian from Center for Biological Imaging (CBI), Institute of Biophysics, Chinese Academy of Sciences, for technical support with LSM980 Confocal-Plus imaging and image analysis.

Data availability

The data supporting the findings of this study are available from the corresponding authors upon request. The RNA-seq data have been deposited in the NCBI Gene Expression Omnibus (GSE289958). Source data for the figures and supplementary figures are provided as a Source Data file. Source data are provided with this paper.

References

1. van Es MA et al (2017) Amyotrophic lateral sclerosis. Lancet 390:2084–2098
2. Akçimen F et al (2023) Amyotrophic lateral sclerosis: translating genetic discoveries into therapies. Nat Rev Genet 24:642–658
3. Park J, Kim J-E, Song T-J (2022) The Global Burden of Motor Neuron Disease: An Analysis of the 2019 Global Burden of Disease Study. Front Neurol 13:864339
4. Xiong L et al (2022) Inflammation-dependent oxidative stress metabolites as a hallmark of amyotrophic lateral sclerosis. Free Radical Bio Med 178:125–133
5. Le Gall L et al (2020) Molecular and Cellular Mechanisms Affected in ALS. J Pers Med 10:101
6. Saccon RA, Bunton-Stasyshyn RKA, Fisher EMC, Fratta P (2013) Is SOD1 loss of function involved in amyotrophic lateral sclerosis? *Brain* 136, 2342–2358
7. Witzel S et al (2022) Safety and effectiveness of long-term intravenous administration of edaravone for treatment of patients with amyotrophic lateral sclerosis. JAMA Neurol 79:121–130
8. Lunetta C et al (2020) The Italian multicenter experience with edaravone in amyotrophic lateral sclerosis. J Neurol 267:3258–3267
9. Shi P, Gal J, Kwinter DM, Liu X, Zhu H (2010) Mitochondrial dysfunction in amyotrophic lateral sclerosis. Bba-Mol Basis Dis 1802:45–51
10. Tapias V, McCoy JL, Greenamyre JT (2019) Phenothiazine normalizes the NADH/NAD+ ratio, maintains mitochondrial integrity and protects the nigrostriatal dopamine system in a chronic rotenone model of Parkinson's disease. Redox Biol 24:101164

11. Liu Y, Shi J (2019) Antioxidative nanomaterials and biomedical applications. Nano Today 27:146–177
12. Sahoo SK, Labhasetwar V (2003) Nanotech approaches to delivery and imaging drug. Drug Discov Today 8:1112–1120
13. Muller RH, Keck CM (2004) Challenges and solutions for the delivery of biotech drugs - a review of drug nanocrystal technology and lipid nanoparticles. J Biotechnol 113:151–170
14. Díaz-García D et al (2022) Design of Mesoporous Silica Nanoparticles for the Treatment of Amyotrophic Lateral Sclerosis (ALS) with a Therapeutic Cocktail Based on Leptin and Pioglitazone. ACS Biomater Sci Eng 8:4838–4849
15. Lu Y et al (2023) Intranasal administration of edaravone nanoparticles improves its stability and brain bioavailability. J Control Release 359:257–267
16. Ediriweera GR et al (2025) Lipid nanoparticles and transcranial focused ultrasound enhance the delivery of SOD1 antisense oligonucleotides to the murine brain for ALS therapy. J Control Release 378:221–235
17. Ali SS et al (2004) A biologically effective fullerene (C-60) derivative with superoxide dismutase mimetic properties. Free Radic Biol Med 37:1191–1202
18. Ding H et al (2020) Carbon-based nanozymes for biomedical applications. Nano Res 14:570–583
19. Huang Y, Ren J, Qu X, Nanozymes (2019) Classification, Catalytic Mechanisms, Activity Regulation, and Applications. Chem Rev 119:4357–4412
20. Valgimigli L, Baschieri A, Amorati R (2018) Antioxidant activity of nanomaterials. J Mater Chem B 6:2036–2051
21. Gao L et al (2007) Intrinsic peroxidase-like activity of ferromagnetic nanoparticles. Nat Nanotechnol 2:577–583
22. Wei H et al (2021) Nanozymes: A clear definition with fuzzy edges. Nano Today 40:101269
23. Zhao H, Zhang R, Yan X, Fan K (2021) Superoxide dismutase nanozymes: an emerging star for anti-oxidation. J Mater Chem B 9:6939–6957
24. Yang J et al (2022) Bioinspired copper single-atom nanozyme as a superoxide dismutase-like antioxidant for sepsis treatment. Exploration 2:20210267
25. Wang D et al (2023) Employing Noble Metal-Porphyrins to Engineer Robust and Highly Active Single-Atom Nanozymes for Targeted Catalytic Therapy in Nasopharyngeal Carcinoma. Adv Mater 36:231003
26. Wang Y et al (2023) Tuning Local Coordination Environments of Manganese Single-Atom Nanozymes with Multi-Enzyme Properties for Selective Colorimetric Biosensing. Angew Chem Int Ed 62:e202300119
27. Wang DJ et al (2021) TiO_2 supported single Ag atoms nanozyme for elimination of SARS-CoV2. Nano Today 40:101243

28. Yang X et al (2023) Modulating Pt nanozyme by using isolated cobalt atoms to enhance catalytic activity for alleviating osteoarthritis. Nano Today 49:101809
29. He W, Wu J, Liu J, Li J (2024) Single-Atom Nanozymes for Catalytic Therapy: Recent Advances and Challenges. Adv Funct Mater 34:2312116
30. Wang A, Li J, Zhang T (2018) Heterogeneous single-atom catalysis. Nat Rev Chem 2:65–81
31. Yang X-F et al (2013) Single-Atom Catalysts: A New Frontier in Heterogeneous Catalysis. Acc Chem Res 46:1740–1748
32. Ding C, Zhu A, Tian Y (2014) Functional Surface Engineering of C-Dots for Fluorescent Biosensing and in Vivo Bioimaging. Acc Chem Res 47:20–30
33. Dhenadhayalan N, Lin K-C, Saleh TA (2020) Recent Advances in Functionalized Carbon Dots toward the Design of Efficient Materials for Sensing and Catalysis Applications. Small 16:1905767
34. Li D, Ushakova EV, Rogach AL, Qu S (2021) Optical Properties of Carbon Dots in the Deep-Red to Near-Infrared Region Are Attractive for Biomedical Applications. Small 17:2102325
35. Shi X et al (2019) Far-Red to Near-Infrared Carbon Dots: Preparation and Applications in Biotechnology. Small, e1901507
36. Zheng XT, Ananthanarayanan A, Luo KQ, Chen P (2015) Glowing Graphene Quantum Dots and Carbon Dots: Properties, Syntheses, and Biological Applications. Small 11:1620–1636
37. Wang X, Lu Y, Hua K, Yang D, Yang Y (2021) Iodine-doped carbon dots with inherent peroxidase catalytic activity for photocatalytic antibacterial and wound disinfection. Anal Bioanal Chem 413:1373–1382
38. Yao L et al (2022) Carbon Quantum Dots-Based Nanozyme from Coffee Induces Cancer Cell Ferroptosis to Activate Antitumor Immunity. ACS Nano 16:9228–9239
39. Wei S-C, Lin Y-W, Chang H-T (2019) Carbon Dots as Artificial Peroxidases for Analytical Applications. J Anal Test 3:191–205
40. Dong C et al (2021) Inhibition of oxidative stress in vivo through enzyme-like activity of carbon dots. Appl Mater Today 25:101178
41. Li F et al (2017) Selenium-Doped Carbon Quantum Dots for Free-Radical Scavenging. Angew Chem Int Ed 56:9910–9914
42. Kong B et al (2022) Carbon dots as nanocatalytic medicine for anti-inflammation therapy. J Colloid Interface Sci 611:545–553
43. Liu C et al (2023) Red Emissive Carbon Dot Superoxide Dismutase Nanozyme for Bioimaging and Ameliorating Acute Lung Injury. Adv Funct Mater 33:2213856
44. Gao W et al (2023) Deciphering the catalytic mechanism of superoxide dismutase activity of carbon dot nanozyme. Nat Commun 14:160
45. Li J et al (2025) Tuning the Excited-State Intramolecular Proton Transfer in Carbon Dots via Coordination with Metal Ion. Inorg Chem 64:7706–7715

46. Pan L, Sun S, Zhang L, Jiang K, Lin H (2016) Near-infrared emissive carbon dots for two-photon fluorescence bioimaging. Nanoscale 8:17350–17356
47. Li Y et al (2012) Discharge product morphology and increased charge performance of lithium–oxygen batteries with graphene nanosheet electrodes: the effect of sulphur doping. J Mater Chem 22:20170–20174
48. Mocci F et al (2022) Carbon nanodots from an in silico perspective. Chem Rev 122:13709–13799
49. Wang Z et al (2021) Accelerated discovery of superoxide-dismutase nanozymes via high-throughput computational screening. Nat Commun 12:6866
50. Cole NB, Daniels MP, Levine RL, Kim G (2010) Oxidative stress causes reversible changes in mitochondrial permeability and structure. Exp Gerontol 45:596–602
51. Xu X, Pang Y, Fan X (2025) Mitochondria in oxidative stress, inflammation and aging: from mechanisms to therapeutic advances. Sig Transduct Target Ther 10:190
52. Huang G et al (2022) Bioactive Nanoenzyme Reverses Oxidative Damage and Endoplasmic Reticulum Stress in Neurons under Ischemic Stroke. ACS Nano 16:431–452
53. De Lorenzo F et al (2023) CDNF rescues motor neurons in models of amyotrophic lateral sclerosis by targeting endoplasmic reticulum stress. Brain 146:3783–3799
54. Zha S, Liu H, Li H, Li H, Wong K-L, All AH (2024) Functionalized nanomaterials capable of crossing the blood–brain barrier. ACS Nano 18:1820–1845
55. Garbuzova-Davis S et al (2012) Impaired blood–brain/spinal cord barrier in ALS patients. Brain Res 1469:114–128
56. Zhong Z et al (2008) ALS-causing SOD1 mutants generate vascular changes prior to motor neuron degeneration. Nat Neurosci 11:420–422
57. Zhou Y et al (2023) Honokiol alleviated neurodegeneration by reducing oxidative stress and improving mitochondrial function in mutant SOD1 cellular and mouse models of amyotrophic lateral sclerosis. Acta Pharm Sin B 13:577–597
58. Ito H et al (2008) Treatment with edaravone, initiated at symptom onset, slows motor decline and decreases SOD1 deposition in ALS mice. Exp Neurol 213:448–455
59. Miyoshi S et al (2017) DOK7 gene therapy enhances motor activity and life span in ALS model mice. EMBO Mol Med 9:880–889
60. Pansarasa O, Rossi D, Berardinelli A, Cereda C (2014) Amyotrophic Lateral Sclerosis and Skeletal Muscle: An Update. Mol Neurobiol 49:984–990
61. Yoo Y-E, Ko C-P (2011) Treatment with trichostatin A initiated after disease onset delays disease progression and increases survival in a mouse model of amyotrophic lateral sclerosis. Exp Neurol 231:147–159
62. Leyton-Jaimes MF, Kahn J, Israelson A (2019) AAV2/9-mediated overexpression of MIF inhibits SOD1 misfolding, delays disease onset, and extends survival in mouse models of ALS. *Proc. Natl. Acad. Sci. USA* 116, 14755–14760

63. Bono S, Feligioni M, Corbo M (2021) Impaired antioxidant KEAP1-NRF2 system in amyotrophic lateral sclerosis: NRF2 activation as a potential therapeutic strategy. Mol Neurodegener 16:71
64. Parvanovova P, Evinova A, Grofik M, Hnilicova P, Tatarkova Z, Turcanova-Koprusakova M (2024) Mitochondrial Dysfunction in Sporadic Amyotrophic Lateral Sclerosis Patients: Insights from High-Resolution Respirometry. Biomedicines 12:1294
65. Joshi AU et al (2018) Inhibition of Drp1/Fis1 interaction slows progression of amyotrophic lateral sclerosis. EMBO Mol Med 10:e8166
66. Wang H et al (2025) Exosome-Functionalized Self-Carrier Enzyme-Like/Drug With Triple Amplified Anti-Oxidative Stress for Synergistic Depression Therapy. Small 21:2411030
67. Cao J et al (2023) ROS filter coating scaffold protects 3D mesenchymal stem cell spheroids for dual-phase treatment of spinal cord injury. Chem Eng J 462:142192
68. Greco V, Longone P, Spalloni A, Pieroni L, Urbani A (2019) Crosstalk Between Oxidative Stress and Mitochondrial Damage: Focus on Amyotrophic Lateral Sclerosis. In: *Mitochondria in Health and in Sickness* (eds Urbani A, Babu M). Springer Singapore
69. Kresse G, Furthmüller J (1996) Efficiency of ab-initio total energy calculations for metals and semiconductors using a plane-wave basis set. Comput Mater Sci 6:15–50
70. Kresse G, Joubert D (1999) From ultrasoft pseudopotentials to the projector augmented-wave method. Phys Rev B 59:1758
71. Blöchl PE (1994) Projector augmented-wave method. Phys Rev B 50:17953
72. Grimme S, Ehrlich S, Goerigk L (2011) Effect of the damping function in dispersion corrected density functional theory. J Comput Chem 32:1456–1465
73. Grimme S, Antony J, Ehrlich S, Krieg H (2010) A consistent and accurate ab initio parametrization of density functional dispersion correction (DFT-D) for the 94 elements H-Pu. J Chem Phys 132:154104
74. Perdew JP, Burke K, Ernzerhof M (1996) Generalized Gradient Approximation Made Simple. Phys Rev Lett 77:3865–3868
75. Kresse G, Hafner J (1993) Ab initio molecular dynamics for liquid metals. Phys Rev B 47:558–561
76. Kresse G, Furthmüller J (1996) Efficient iterative schemes for ab initio total-energy calculations using a plane-wave basis set. Phys Rev B 54:11169–11186
77. Yang B et al (2023) NRF2 activation suppresses motor neuron ferroptosis induced by the SOD1G93A mutation and exerts neuroprotection in amyotrophic lateral sclerosis. Neurobiol Dis 184:106210
78. Martin MJE (2011) j. Cutadapt removes adapter sequences from high-throughput sequencing reads. EMBnet J 17:10–12
79. Kim D, Paggi JM, Park C, Bennett C, Salzberg SL (2019) Graph-based genome alignment and genotyping with HISAT2 and HISAT-genotype. Nat Biotechnol 37:907–915
80. Robinson MD, McCarthy DJ, Smyth GK (2010) edgeR: a Bioconductor package for differential expression analysis of digital gene expression data. Bioinformatics 26:139–140

81. Chen C et al (2023) TBtools-II: A one for all, all for one bioinformatics platform for biological big-data mining. Mol Plant 16:1733–1742
82. Huang D, Sherman B, Lempicki R (2009) Systematic and integrative analysis of large gene lists using DAVID bioinformatics resources. Nat Protoc 4:44–57

Figures

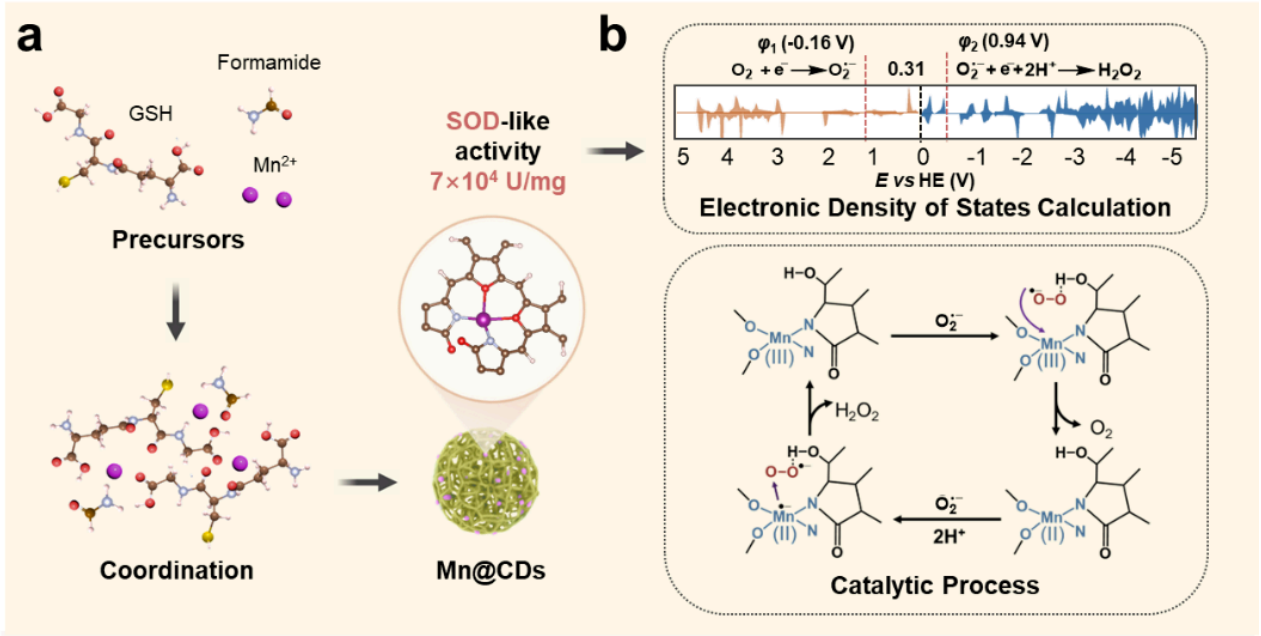

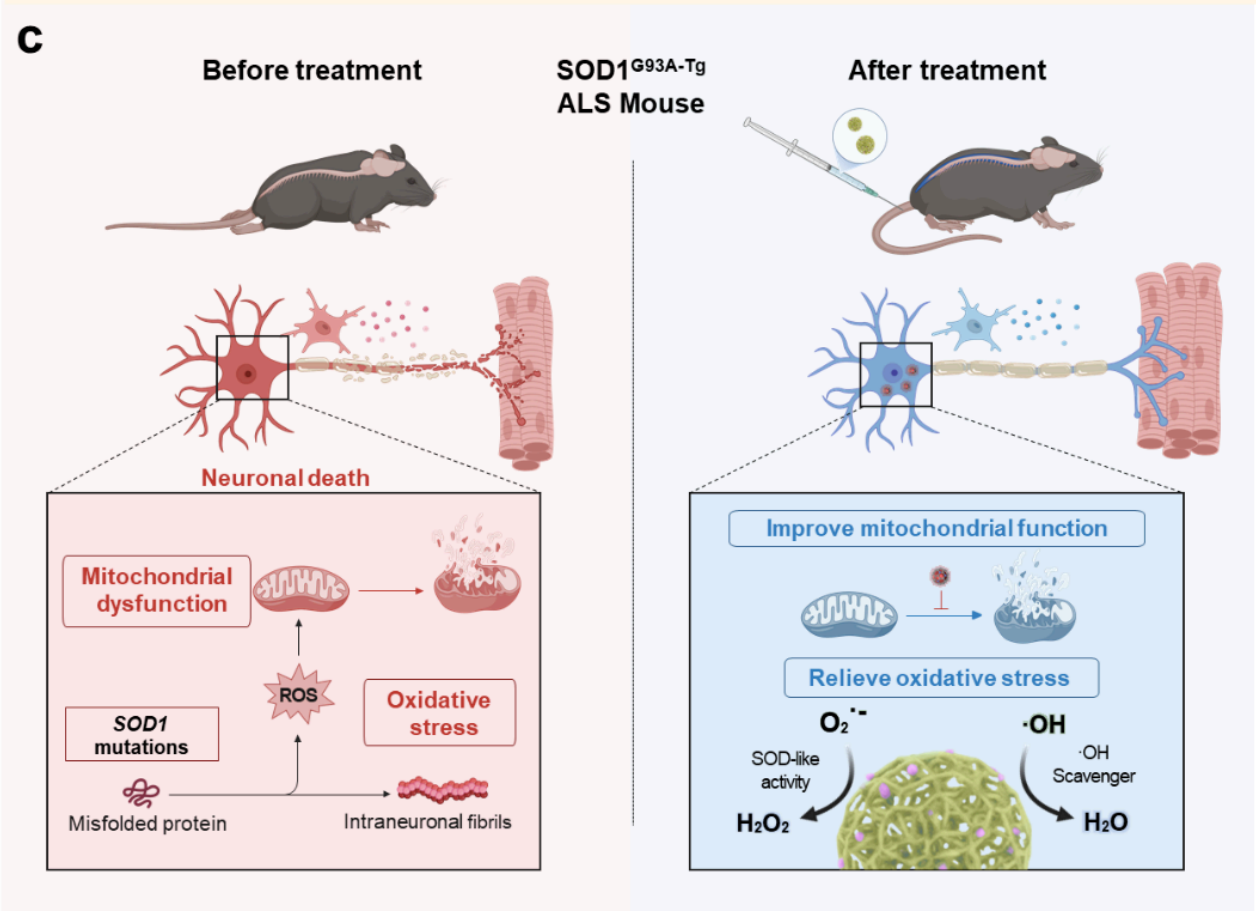

Figure 1

Design and mechanism of Mn@CDs.

aThe illustration of the synthesis process of Mn@CDs. **b** The proposed catalytic mechanism of Mn@CDs. **c** The therapeutic effects and mechanisms of Mn@CDs in ALS models.

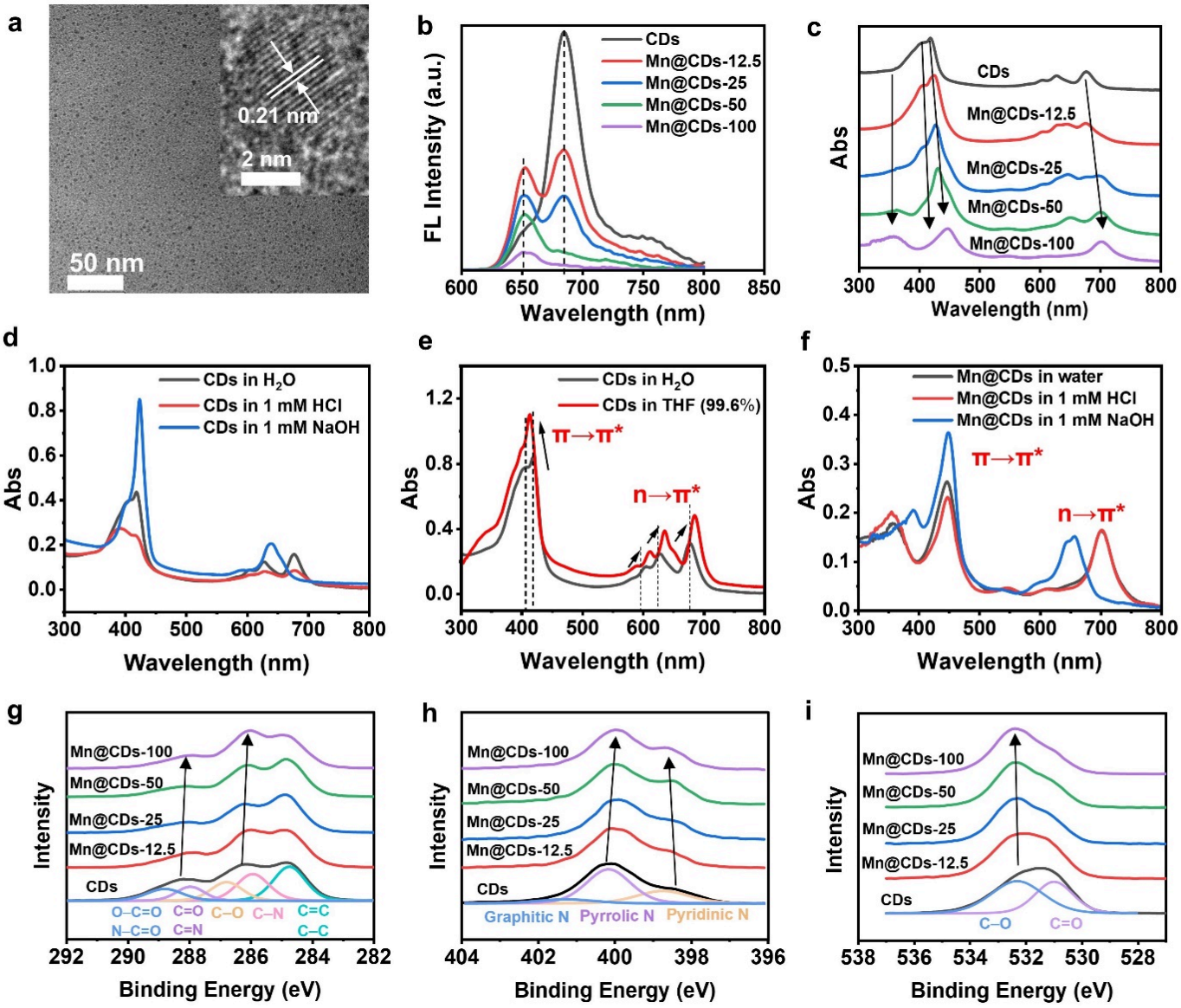

Figure 2

Structural characterization of the Mn@CDs.

a Representative TEM image of the Mn@CDs. **b-c** fluorescence spectra (**b**), and UV-vis absorption spectra (**c**) of the CDs and Mn@CDs. **d** The UV-vis absorption spectra of CDs (final concentration of 10 μg/mL) in water, 1 mM HCl, and 1mM NaOH. e The UV-vis absorption spectra of CDs (final concentration of 20 μg/mL) in water, and THF (99.6%). f The UV-vis absorption spectra of Mn@CDs-100 (final concentration of 10 μg/mL) in water, 1 mM HCl, and 1mM NaOH. g-i C 1s (**g**), N 1s (**h**), and O 1s (**i**) high

resolution XPS spectra with identification of peaks by curve fitting of CDs and Mn@CDs as indicated. Source data are provided as a Source Data file.

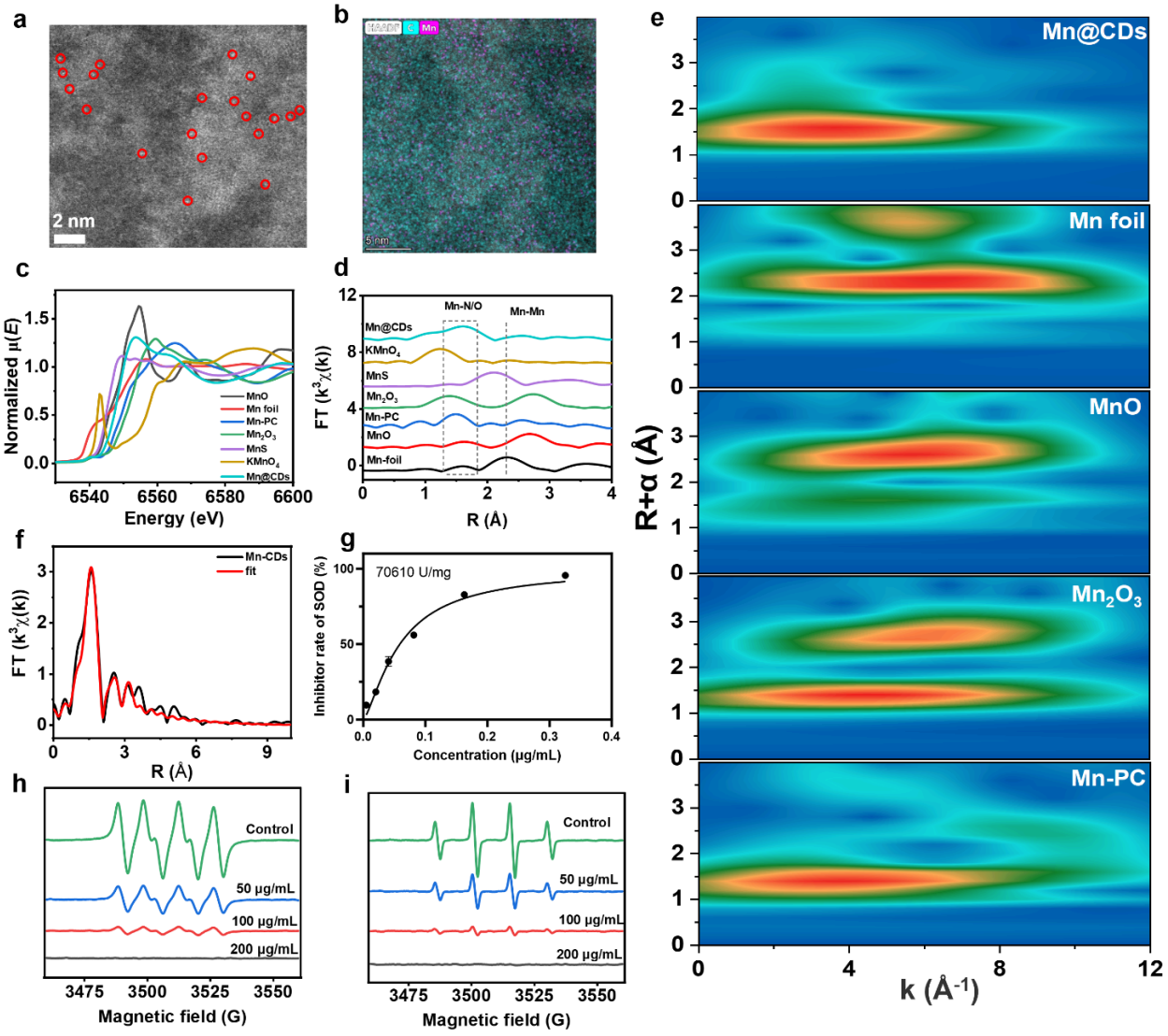

Figure 3

Fine structure and SOD-like activity of the Mn@CDs.

a-b HAADF-STEM image (**a**) and EDS mapping (**b**) of the Mn@CDs. **c** Normalized Mn K-edge XANES spectra, **d** k3-weighted FT-EXAFS spectra, and **e** Corresponding WT plots of Mn foil, MnO, Mn_2O_3, MnPc, and Mn@CDs. **f** The corresponding EXAFS fitting curves in R-space with magnitude and imaginary parts for Mn@CDs. **g** Illustration of the SOD-like activity of Mn@CDs. **h-i** $O_2^{\bullet-}$ scavenging capacity (**h**) and $^{\bullet}OH$ scavenging capacity (**i**) of the Mn@CDs. Source data are provided as a Source Data file.

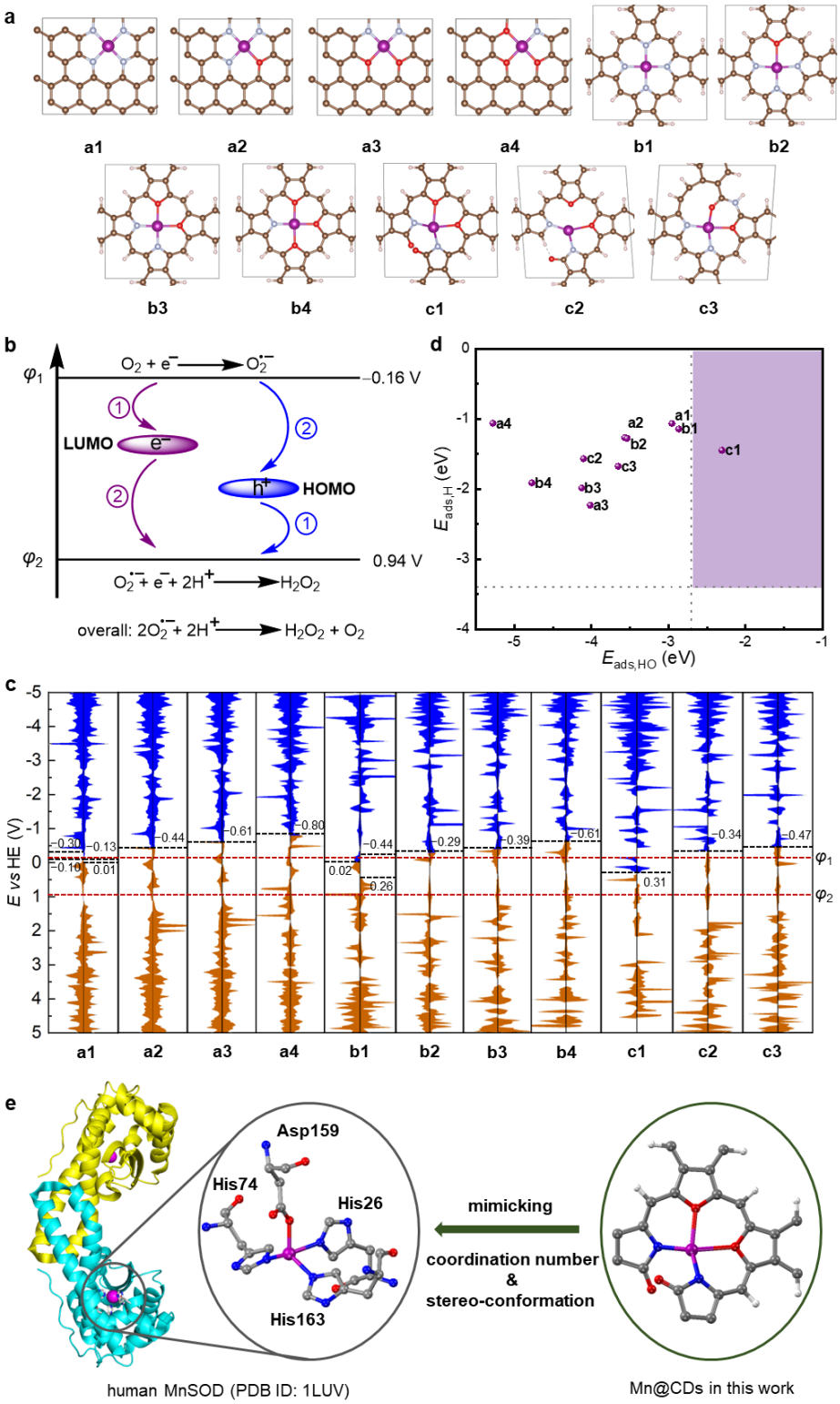

Figure 4

Theoretical calculation results.

a Periodic structural models representing different active centers of Mn@CDs. **b** Intermediate frontier molecular orbital model illustrating the catalytic activity of superoxide dismutase, with φ_1 and φ_2 denoting the reduction potentials of O_2/ $O_2^{\bullet-}$ and $O_2^{\bullet-}$, H^+/H_2O_2 at pH = 7. **c** Electronic density of states

calculations showing the energy levels of FMOs, including the valence band maximum, conduction band minimum (CBM), and Fermi level. **d** Calculated adsorption energies (E_{ads}) for HO* and H* on the models in **a**, with regions highlighted in purple indicating the partition function where $x_{SOD} > 0.5$. **e** The activity site of Mn@CDs. Source data are provided as a Source Data file.

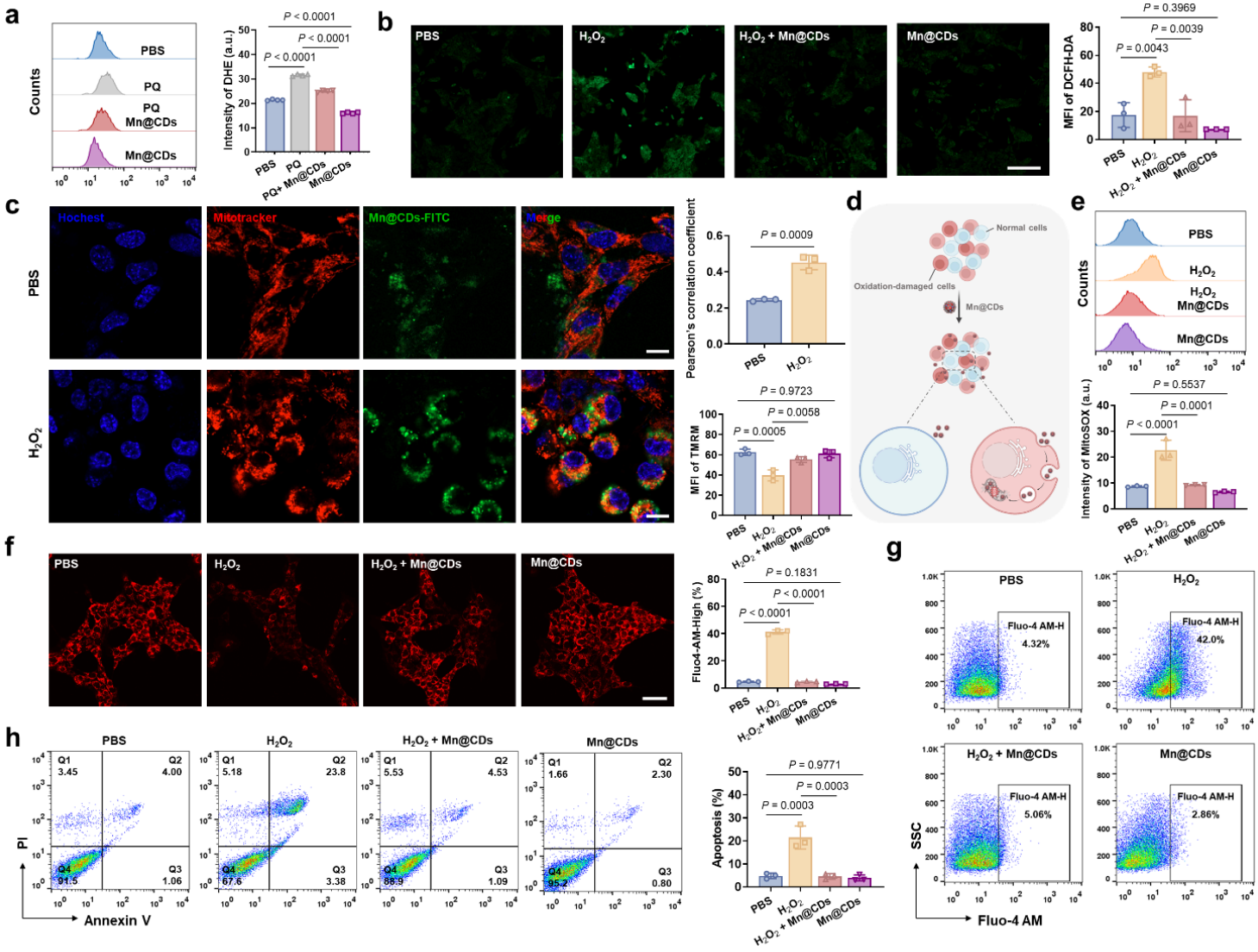

Figure 5

Protective effects of the Mn@CDs on NSC-34 cells against ROS-induced damage.

a Flow cytometry analysis of $O_2^{\bullet-}$ levels in NSC-34 cells subjected to different treatments detected by the fluorescent probe DHE and quantification of the fluorescence intensity (n = 4). **b** Representative fluorescence images of ROS levels in NSC-34 cells subjected to the indicated treatments stained with DCFH-DA and quantification of the fluorescence intensity of DCFH-DA (n = 3). Scale bar = 200 μm. **c** Representative confocal images and quantification of the Pearson's correlation coefficient showing the enhanced cellular internalization and colocalization of FITC-labeled Mn@CDs (green) with mitochondria (red) under 400 μM H_2O_2 stimulation. The nuclei were stained with Hoechst (blue) (n = 3). Scale bar = 10

μm. **d** Illustration of the ability of the Mn@CDs to accumulate in oxidatively damaged cells. This figure was created with BioRender.com and Servier Medical Art (http://smart.servier.com) **e** Detection of mitochondrial ROS levels in NSC-34 cells subjected to different treatments via the fluorescent probe MitoSOX Green via flow cytometry and the corresponding quantitative analysis of the fluorescence intensity (*n* = 3). **f** Representative TMRM staining images showing the mitochondrial membrane potential of NSC-34 cells after the indicated treatments and quantification of the fluorescence intensity (*n* = 3). Scale bar = 50 μm. **g** Comparison of the calcium concentration in NSC-34 cells after the indicated treatments by Fluo-4 AM staining and quantification of the percentage of Ca^{2+} positive cells (*n* = 3). **h** Evaluation of cell apoptosis via flow cytometry analysis via Annexin V-FITC/PI staining and quantification of the apoptosis rate (*n* = 3). All the quantification data are presented as the means ± SDs in (**a-c** and **e-h**). *P* values were determined via one-way ANOVA. Source data are provided as a Source Data file.

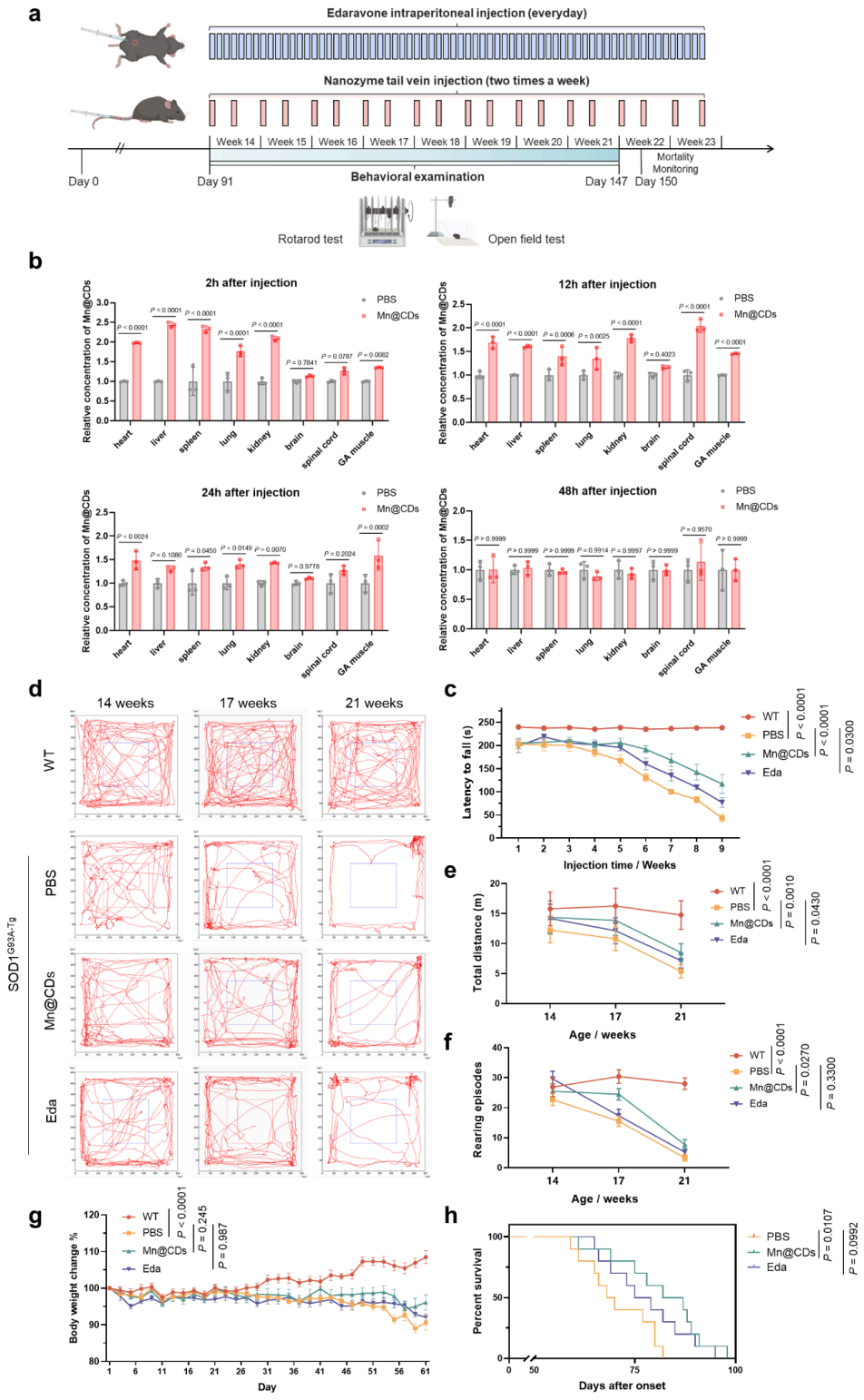

Figure 6

Ameliorative effects of the Mn@CDs on motor function and survival in the ALS mouse model.

a Schematic illustration of the experimental process of *in vivo* studies. This figure was created with BioRender.com and Servier Medical Art (http://smart.servier.com). **b** ICP–MS analysis was used to evaluate the accumulation of Mn@CDs in the spinal cord of SOD1$^{G93A\text{-}Tg}$ mice (n = 3). **c** Latency to fall

during the rotarod test in the WT group and the SOD1$^{G93A\text{-}Tg}$ mice in the PBS, Mn@CDs, and Eda groups (n = 10). **d** Representative tracks of the mice in the indicated groups in the open field test at 14, 17, and 21 weeks (n = 10). **e, f** Total distance traveled (**e**) and number of rearing episodes (**f**) in the open field test at different weeks (n = 10). **g** Body weight changes of the mice in the different groups throughout the treatment period (n = 10). **h** Survival analysis of mice subjected to different treatments (n = 10). All the quantification data are presented as the means ± SDs in (**b**) , (**c**) and (**e-g**). P values were determined via two-way ANOVA for (**b**), repeated-measures ANOVA followed by post hoc LSD tests for (**c**), (**e**), (**f**), and Kaplan–Meier analysis with the log-rank test for (**h**). Source data are provided as a Source Data file.

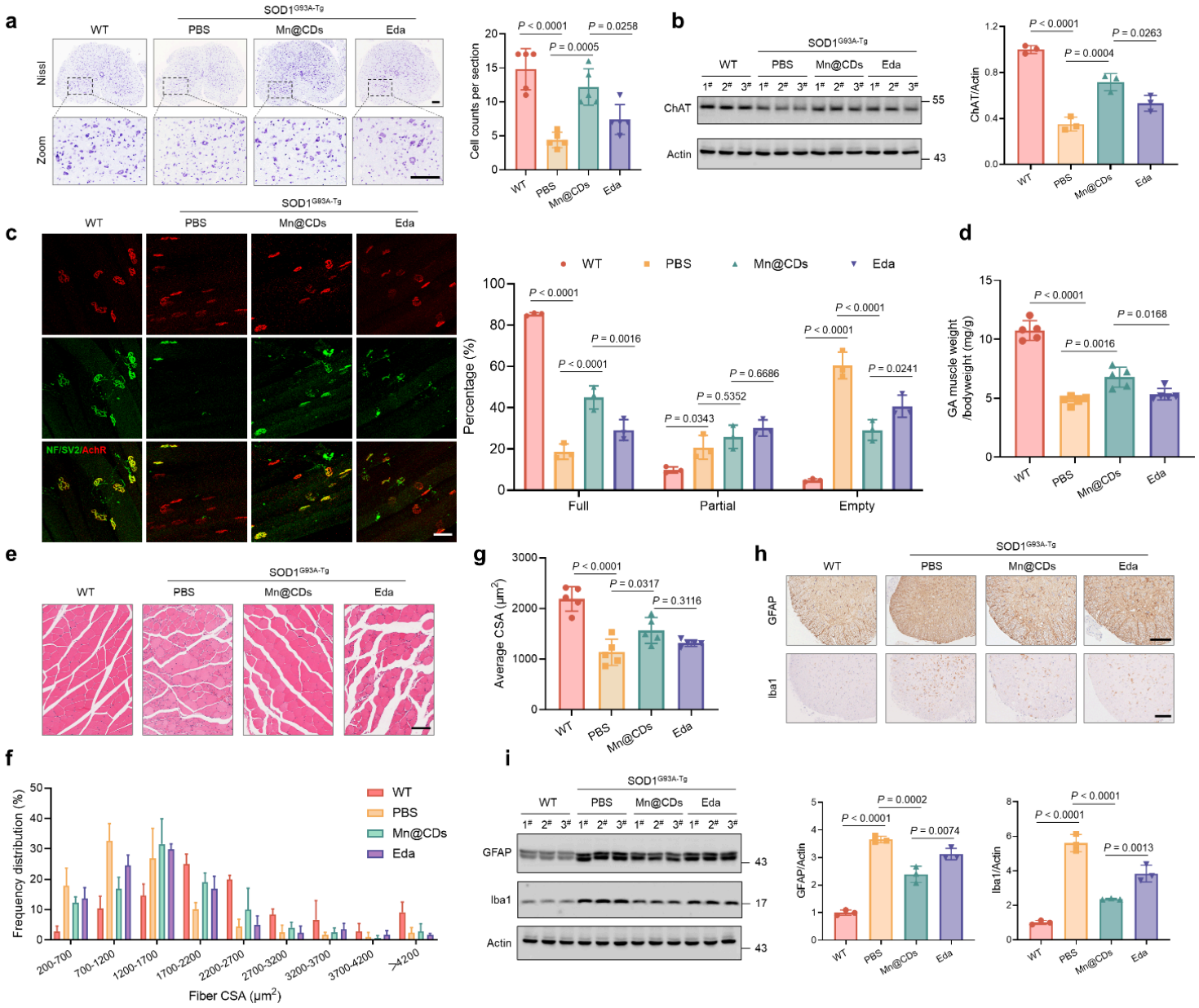

Figure 7

Alleviation effect of Mn@CDs on the impairment of neurons and motor units in the ALS mouse model.

a Representative Nissl-stained images and quantification of large motor neurons in lumbar spinal cord sections from WT mice and SOD1$^{G93A\text{-}Tg}$ mice treated with PBS, Mn@CDs, or Eda (*n* = 5). Scale bar = 100 μm. **b** Immunoblot analysis of the expression level of ChAT and relative quantification in the lumbar spinal cord lysates of mice subjected to different treatments. Actin was used as an internal control. The relative abundance of ChAT to Actin was normalized to that of the WT group (*n* = 3). **c** Representative NMJ immunofluorescence images gastrocnemius muscle (GA) sections from the indicated groups. Scale bar = 50 μm. For quantification, 5 microscopic fields were chosen at random on the diaphragm muscle from each mouse, and 150–250 synaptic sites were analyzed per mouse. The NMJs were categorized as fully innervated, partially innervated, or empty. Motor endplates are identified with α-bungarotoxin (red); axons are identified with neurofilament + SV2 (green) (*n* = 3). **d** Mass of GA muscles in different groups (*n* = 5). **e** Representative hematoxylin and eosin (H&E) staining images of GA muscle sections. Scale bar = 100 μm. **f, g** Size distribution of the CSA (**f**) and average CSA (**g**) of GA muscle sections (*n* = 5). **h** Representative images of immunohistochemical staining for GFAP and Iba1 in lumbar spinal cord sections from the indicated groups. Scale bar = 100 μm. **i** Evaluation of the expression levels of GFAP and Iba1 in lumbar spinal cord lysates from each group via immunoblot analysis and relative quantification. Actin was used as an internal control. The relative abundance of GFAP and Iba1 to Actin was normalized to that in the WT group (*n* = 3). All the quantification data are presented as the means ± SDs in (**a**-**d**), (**f**), (**g**), and (**i**). The *P* value was determined via one-way ANOVA in (**a**-**d**), (**g**), and (**i**). Source data are provided as a Source Data file.

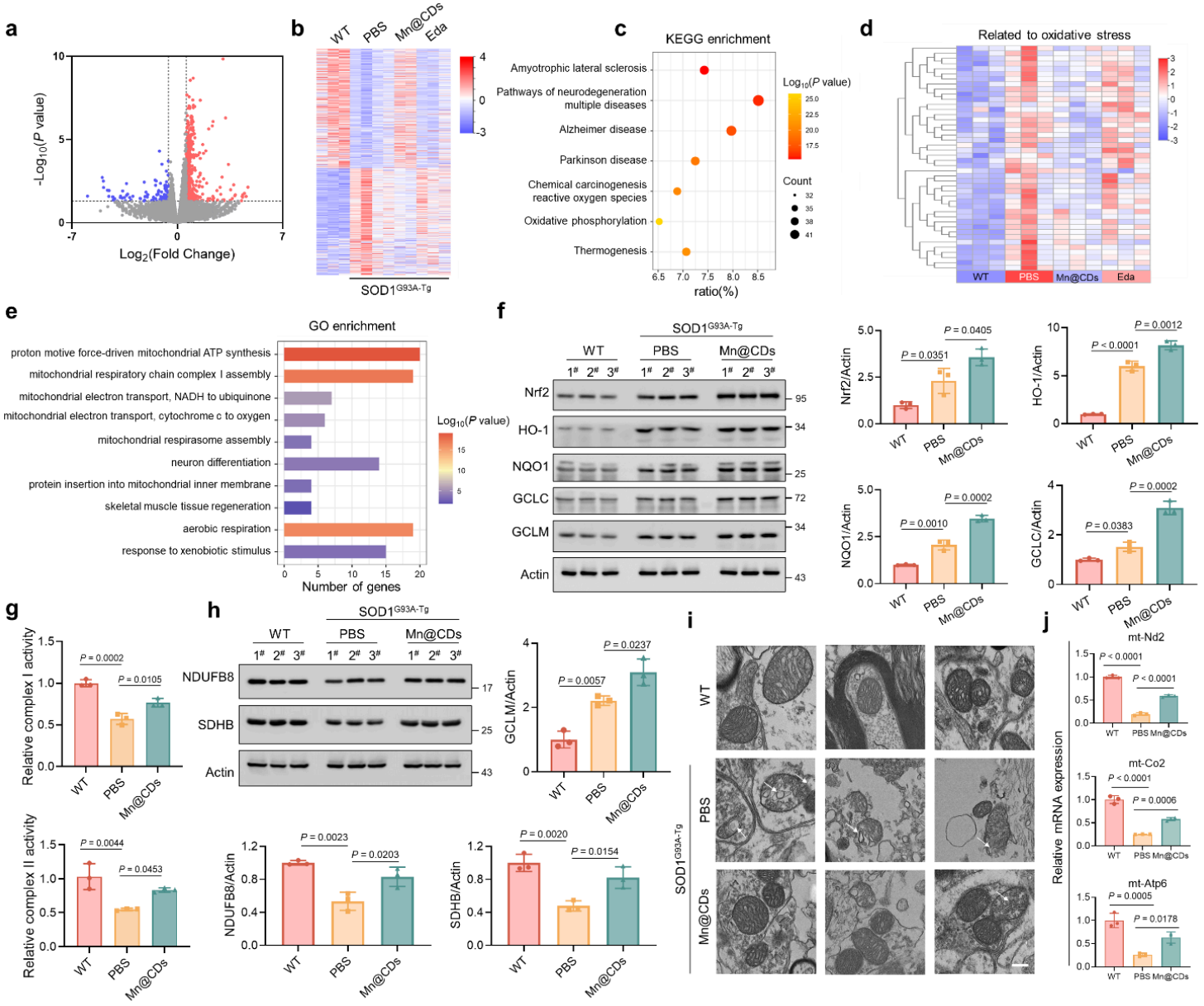

Figure 8

Recovery effect of the Mn@CDs against oxidative stress and mitochondrial dysfunction.

a Volcano plot showing the differentially expressed genes (DEGs) between the lumbar spinal cord samples of SOD1$^{G93A-Tg}$ mice treated with PBS or Mn@CDs in the RNA-seq data. The red and blue dots represent up- and downregulated DEGs, respectively (*n* = 3). **b** Heatmap analysis of the DEGs in WT mice and SOD1$^{G93A-Tg}$ mice treated with PBS, Mn@CDs, or Eda. **c** KEGG disease enrichment analysis of the DEGs from (**b**). **d** Heatmap analysis of the DEGs related to the response to oxidative stress in groups with different treatments. **e** GO pathway enrichment analysis of the DEGs from (**b**). **f** Immunoblot analysis of the expression levels of Nrf2, HO-1, NQO1, GCLC, and GCLM and relative quantification in the indicated groups. Actin was used as an internal control. The relative abundance of these proteins to that of Actin was normalized to that of the WT group. (*n* = 3). **g** Relative activity of mitochondrial respiratory

complexes I and II in the indicated groups (*n* = 3). **h** Immunoblot analysis of the expression levels of NDUFB8 and SDHB and relative quantification in the indicated groups. Actin was used as an internal control. The relative abundance of these proteins to that of Actin was normalized to that of the WT group (*n* = 3). **i** Representative transmission electron microscopy images of the mitochondria in lumbar spinal cord samples from the indicated groups (*n* = 5). The white arrows indicate mitochondria with vacuolation or broken cristae. Scale bar = 500 nm. **j** qPCR analysis of the mRNA levels of representative mitochondrially encoded genes in the lumbar spinal cord lysates of the mice in the different groups. The *ACTIN* gene was used as an internal control (*n* = 3). All quantification data are presented as the mean ± SDs in (**f**-**j**), and the *P* value was determined via one-way ANOVA in (**f**-**j**). Source data are provided as a Source Data file.

Supplementary Files

This is a list of supplementary files associated with this preprint. Click to download.

- NCSupplementaryMaterialshighlight0214.docx
- rsnew.pdf
- Sourcedata20260210.xlsx